이학박사 학위논문

Variational approach in image restoration problems

(영상 복원 문제의 변분법적 접근)

2013년 2월

서울대학교 대학원

수리과학부

오 승 미

Variational approach in image restoration problems

(영상 복원 문제의 변분법적 접근)

지도교수 강 명 주

이 논문을 이학박사 학위논문으로 제출함

2012년 10월

서울대학교 대학원

수리과학부

오 승 미

오 승 미의 이학박사 학위논문을 인준함

2012년 12월

위 원 장 _____ (인)

부 위 원 장 _____ (인)

위 원 _____ (인)

위 원 _____ (인)

위 원 _____ (인)

Variational approach in image restoration problems

A dissertation
submitted in partial fulfillment
of the requirements for the degree of
Doctor of Philosophy
to the faculty of the Graduate School of
Seoul National University

by

Seungmi Oh

Dissertation Director : Professor Myungjoo Kang

Department of Mathematical Sciences
Seoul National University

February 2013

Abstract

Image restoration has been an active research area in image processing and computer vision during the past several decades. We explore variational partial differential equations (PDE) models in image restoration problem. We start our discussion by reviewing classical models, by which the works of this dissertation are highly motivated. The content of the dissertation is divided into two main subjects. First topic is on image denoising, where we propose non-convex hybrid total variation model, and then we apply iterative reweighted algorithm to solve the proposed model. Second topic is on image decomposition, in which we separate an image into structural component and oscillatory component using local gradient constraint.

Key words: image restoration, variational method, Euler-Lagrange equation, image denoising, image decomposition
Student Number: 2004-23262

Contents

List of Figures

Chapter 1

Introduction

There are various approaches to remove image artifacts and improve image quality. They have been developed in very various fields of mathematics, engineering, and statistics. To my best knowledge, stochastic filters, wavelets, sparse and redundant representation, and variational approaches are considered as successful research directions. Stochastic modeling and wavelet-based approaches have been intensively researched for several decades. But, sparse and redundant representation is relatively young and is considered as a new trend. This field is based on the fact that image contents can be represented sparsely and introduces the concept of dictionaries replacing the traditional wavelet presentation. Variational approaches are founded on solving PDE derived from minimizing an energy functional, which typically consists of a regularization term and a data fidelity term.

Variational and PDE based image restoration models have had great success in the past 20 years. Our main research interest also lies in the variational approaches. In this dissertation, we deal with variational approaches in image restoration problem where the image u is computed by minimizing an energy functional. In other words, the minimizer u is the solution of the corresponding Euler-Lagrange equation. The success of variational model depends on the selection of an appropriate regularizer, which is achieved by manipulating image derivatives.

1.1 Image restoration

We consider classical problems in image restoration. Given a blurry and noisy image $f : \Omega \to R$, the standard linear degradation model that relates f to u is

$$f = K * u + n \tag{1.1.1}$$

where Ω is a bounded open subset on R^2, K is a convolution kernel with compact support, u is the original image and n is Gaussian white noise.

Under the above image restoration problem formulation, we want to recover the unknown u from the given image f. This is a representative inverse problem. Since there are infinitely many possible solutions, additional criteria are needed to guarantee a well-defined solution. In a variational framework, these criteria are regularization. The solutions of the above problem are presented as minimizers of a proper energy functional and a regularizer must be chosen to evaluate the restored solution with smaller costs. From necessary optimality condition, we can derive corresponding PDE, which are called Euler-Lagrange equations.

Variational approaches have been extensively developed in wide range of image restoration tasks such as image denoising, deblurring, blind deconvolution, segmentation, inpainting, decomposition and so on. When K is a blurring operator, the image restoration problem (1.1.1) becomes deblurring. The operator K could be the identity, in which case the problem reduces to denoising. The K representing a down-sampling operator leads to super-resolution. The masking of some pixels K produces inpainting and a set of random projections K corresponds compressed sensing.

Given knowledge of the kernel K and the noise, one of the most successful approaches to solve this problem is the total variation (TV) regularization method (ROF model) [59], $\phi(x) = x$. Authors solved the following constrained minimization problem:

$$\min_u \int_\Omega \phi(|\nabla u|) + \frac{\mu}{2} \int_\Omega (K * u - f)^2 \tag{1.1.2}$$

where μ is a scale parameter. There are numerical methods for solving the above nonlinear type PDE; time marching schemes [59], lagged diffusivity

fixed point schemes [69], primal-dual method [20] and split Bregman method [34] etc.

We can think of recovering the true image u and kernel K without knowing any priori knowledge of u and K. In this case, called blind deconvolution, it is more sophisticated than the above case.

Many models in this dissertation are based on TV. We focus on image denoising and image decomposition.

1.2 Brief overview of the dissertation

In this section, we briefly overview this dissertation. Chapter 2 is devoted to survey a classical image restoration model. Since Rudin et. al introduced TV as a regularizer in [59], there have been intensive researches. These works are highly motivated by researches based on TV.

Main contributions of this dissertation are twofold. Chapter 3 concerns the first contribution. In this chapter, we propose a novel variational model. The key idea is the introduction of non-convexity of higher order TV as well as TV. In order to obtain the combined benefits of two regularizers and to overcome their demerits, we propose the use of a convex combination of non-convex TV and non-convex higher order TV (HOTV) as regularizers for the image denoising problem. The non-convexity and non-smoothness are difficulties of the proposed model to be solved numerically. Hence we use an iterative reweighted minimization scheme to solve our proposed model. All numerical experiments demonstrate the efficiency and stability of our proposed model.

Second contribution is addressed in chapter 4. We consider TV-Hilbert model as blur and deblur process and add the local gradient constraint to an existing TV-X type model. Numerical results demonstrate that this constraint is a great help to remedy TV-X type model's shortcomings.

In chapter 5, we give the conclusion of this dissertation and discuss the future works.

The content of this thesis in chapter 3 is based on the paper [53].

Chapter 2

Previous works

Variational models have achieved success in various image restoration tasks. But, this thesis's scope encompasses the fundamental problem of image denoising and decomposition.

2.1 Image denoising

Image denoising is a fundamental problem in image processing. It is in charge of a significant preliminary step in many image processing and computer vision tasks. This problem aims to remove noises and preserve edges and small scale structures such as textures. In image denoising, it is important to choose an appropriate regularizer in the variational framework and a suitable prior in the statistical framework. By now, we consider a process of remarkable achievement in image denoising problem.

2.1.1 Fundamental model

Since originally Tikhonov [66] suggested $\int_\Omega |\nabla u|^2$ regularizer, it is widespread due to the fact that it reduces the unique and closed form solution. It is also called Wiener filter. But, this regularizer is not the best choice. It smooths images too much and thus, step edges are not allowed. In Figure 2.1, one dimensional step edge is illustrated for intrinsic motivation.

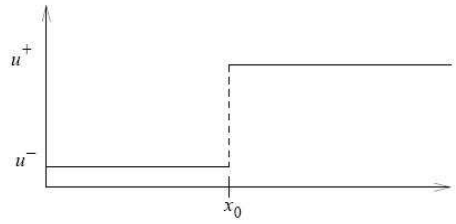

(a)

Figure 2.1: Step function

u is not differentiable at x_0, because $\lim_{h\to 0} \dfrac{u^+ - u^-}{2h} = \infty$.

$$\int_{x_0-h}^{x_0+h} u_x^2 dx = \lim_{h\to 0} \int_{x_0-h}^{x_0+h} \frac{(u^+ - u^-)^2}{4h^2} dx = \lim_{h\to 0} \frac{(u^+ - u^-)^2}{2h} = \infty \quad (2.1.1)$$

Since a step edge which Tikhonov regularizer measures, contributes with infinite energy in (2.1.1) and we look for finite energy results, it is forbidden.

In designing the image denoising model, it is significant issue to preserve image features such as edges, which are easily detected by the human visual system. Since Rudin et al. [59] proposed TV as an image regularizer, there have been impressive achievements in the variational model approach. The formulation for the Rudin-Osher-Fatemi (ROF) model is as follows:

$$\min_{u\in BV(\Omega)} \int_\Omega |\nabla u| + \frac{\mu}{2} \int_\Omega (u - f)^2 \quad (2.1.2)$$

where Ω is a bounded domain in R^2 with a Lipschitz boundary, $BV(\Omega)$ is the space of functions with bounded variation, and $\int_\Omega |\nabla u| = \int_\Omega \sqrt{(u_x)^2 + (u_y)^2}$ is the isotropic TV of u. We can also consider the anisotropic TV of u, $\int_\Omega |u_x| + |u_y|$, but in this thesis, we mainly focus on isotropic TV, and TV hereafter refers to the isotropic TV unless stated otherwise. As it is well known, TV can remove noises and simultaneously preserve edges and meaningful features.

Let us consider one dimensional step edge in Figure 2.1 again.

$$\int_{x_0-h}^{x_0+h} |u_x| dx = \lim_{h\to 0} \int_{x_0-h}^{x_0+h} \frac{u^+ - u^-}{2h} dx = \lim_{h\to 0} u^+ - u^- = u^+ - u^- \quad (2.1.3)$$

In contrast to Tikhonov regularizer, a step edge contributes with finite energy with a new regularizer TV in (2.1.3), so it is allowed. This is a simple example that explains why TV can preserve edges.

Since many researchers have carefully analyzed the ROF model, theoretical results have been accumulated and diverse extensions have been developed. I can not cover all well-structured theory and extensions in this thesis. Instead, I pretend to introduce some basic properties and developments related to the ROF model. It is worth noting that there are extensive works of the ROF model including theoretical results, numerical algorithms and experimental results.

Theorem 2.1.1. *There exists a unique solution $u \in BV(\Omega)$ to the above minimization problem (2.1.2)*

We can derive Euler-Lagrange equation of (2.1.2) from necessary optimality condition.

$$-\nabla \cdot (\frac{\nabla u}{|\nabla u|}) + \mu(u - f) = 0 \tag{2.1.4}$$

This nonlinear PDE is difficult to solve due to the degeneracy of $|\nabla u|$. Originally, many researchers used the smoothed TV $|\nabla u|_\beta = \sqrt{|\nabla u|^2 + \beta}$ to avoid the unstability of $|\nabla u|$. And then they went on the gradient descent direction by introducing an artificial time variable.

$$u_t = -g(u) = \nabla \cdot (\frac{\nabla u}{|\nabla u|_\beta}) - \ \mu(u - f) \tag{2.1.5}$$

But this time marching method is so slow due to CFL condition. To speed up, Marquina et al. [47] used a preconditioning technique by multiplying $|\nabla u|$ and Vogel et al. [69] invented fixed point iteration scheme to achieve linear convergence rate. Chan et al. [20] first introduced duality-based minimization and Chambolle [16] proposed a projection approach to result in global convergence for any initial without smooth parameter β and Lagrange multiplier λ. Recently, new computational methods based upon a convex optimization have been invented with improved robustness and computational cost.

However, in the presence of noises, TV may cause staircase artifacts i.e., smooth transition regions in the intensity tend to be oversegmented to form constant stairs.

2.1.2 Higher order model

The TV is a borderline of convexity; it is convex and linear at infinity. Because of this property, on the one hand, TV is able to reconstruct images with discontinuities, but on the other, TV often leads to staircase effects. The resulting images appear cartoon-like and unnatural. A natural way to alleviate these artifacts is to interpolate TV and H^1 norm to adapt the behavior of $|\nabla u|$. In [10, 11], it was designed by $\int_\Omega |\nabla u|^{p(|\nabla u|)}$ adaptively such that the gradient-driven function $p(x)$ has value 1 near the edges and it is close to value 2 in smooth regions.

To introduce higher order derivative information into the energy [21, 44] is another approach to overcome staircase artifacts. Originally, Lysaker et al. [44] proposed the following Lysaker-Lundervold-Tai (LLT) model:

$$\min_u \int_\Omega |\nabla^2 u| + \frac{\mu}{2} \int_\Omega (u - f)^2 \tag{2.1.6}$$

where $\int_\Omega |\nabla^2 u| = \int_\Omega \sqrt{u_{xx}^2 + u_{xy}^2 + u_{yx}^2 + u_{yy}^2}$ is the HOTV of u. The advantage of this model is its ability to process signals with smooth changes in the intensity. The close approximation of smooth transition regions by higher order derivatives can remove staircase artifacts to a remarkable degree. However, the numerical computation of the LLT model is difficult owing to its non-linearity and non-differentiability, which are also problems of the ROF model. Optimization techniques can be used to efficiently solve the LLT model [73].

Recently, many researchers have shared new insights into the importance of higher order derivatives [8, 12, 40, 76, 79, 81] to overcome the limitation of TV. In [79], authors proposed a new variational model composed of the TV of mean curvature as a regularizer and L_2 data fidelity term. And then they developed a fast algorithm using augmented Lagrangian method [81]. This model showed outstanding capabilities doing noise removal while keeping image contrast, object edges and corners. In [40], the Frobenius norm and spectral norm of the image-Hessian matrix are justified as an appropriate extension of TV, showing that they can restore better the image with smooth intensity changes like biomedical images as well as inherit attractive properties of TV, convexity and rotation invariance etc. Furthermore, the

equivalence between the Hessian Frobenius norm and the L_2 norm of $D^2_{\theta,\phi}u$, where $D^2_{\theta,\phi}u$ is the second directional derivative along angles θ and ϕ, upholds the validity of these regularizer. Meanwhile, the total generalized variation including higher order derivative as a more general model was proposed [12] and enhanced by Bregman iteration [8]. Now, we will deal with this higher order model [12] in detail.

Total generalized variation

In [12, 18, 38], authors suggested the total generalized variation (TGV) model. Since TGV is equivalent to TV for piecewise constant image, it can preserve edges while removing noises. What's more, it can also be applied to wide range of images that include smooth transition regions.

The idea of TGV is simple, that incorporates smoothness information from first up to the k-th derivative of image. When we set $k = 1$ and $\alpha_0 = 1$, it is equivalent to the TV.

$$\begin{aligned}\mathrm{TGV}^k_\alpha(u) = \sup \quad \{ \quad & \int_\Omega u div^k v dx \mid v \in C^k_c(\Omega, Sym^k(R^d)), \\ & \|div^l v\|_\infty \le \alpha_l,\ l = 0, \cdots, k-1\}\end{aligned} \tag{2.1.7}$$

where $\alpha = (\alpha_0, \cdots, \alpha_{k-1}) > 0$ is weights.

It is equivalent to a k-fold infimal convolution of inf-L^1-type functionals evaluated at $\nabla^k u$ and has a well-developed mathematical theory ; see [12]. In this brief introduction of TGV, we restrict our interest to TGV of second order (TGV^2) [38].

$$\mathrm{TGV}^2_\alpha(u) = \inf_{v \in BD(\Omega)} \alpha_1 \int_\Omega |\nabla(u) - v| + \alpha_0 \int_\Omega |\varepsilon(v)| \tag{2.1.8}$$

where $\varepsilon(v) = \frac{1}{2}(\nabla v + \nabla v^\top)$.

It balances optimally between ∇u and $\nabla^2 u$ to avoid staircase artifacts and prefers piecewise smooth images. If ∇u is smooth and $\nabla^2 u \ll \nabla u$, v locally approximates ∇u and TGV^2_α measures $\alpha_0 \int_\Omega |\varepsilon(v)|$. When u jumps, v is approximately zero and TGV^2_α measures $\alpha_1 \int_\Omega |\nabla(u)|$. Therefore, we can say that TGV^2_α adapts to the smoothness of u up to the order 2.

To observe the effect of TGV^2, we introduce TGV^2_α-based denoising model.

$$\min_u \mathrm{TGV}^2_\alpha(u) + \frac{1}{2\lambda} \int_\Omega (u - f)^2 \quad \text{(Primal)} \tag{2.1.9}$$

Knoll et al. [38] employed a first-order primal-dual algorithm [18] for solving TGV^2 denoising model (2.1.9).

$$\min_{u,v}\max_{p,q} < \nabla u - v, p > + < \varepsilon(v), q > + \frac{1}{2\lambda}\|u-f\|_2^2 - \delta_P(p) - \delta_Q(q)) \text{ (Primal-Dual)} \tag{2.1.10}$$

where $P = \{p \in C^{2MN} \mid \|p\|_\infty \leq \alpha_1\}, Q = \{q \in C^{3MN} \mid \|q\|_\infty \leq \alpha_0\}$.

They consider a convex-concave saddle-point structure (2.1.10) which is derived by duality. The optimality condition directly leads to a following algorithm :

Algorithm 1:Primal-dual method for TGV2 denoising

Initialization : $u, \bar{u} \leftarrow f,\ v, \bar{v} \leftarrow 0,\ p \leftarrow 0, q \leftarrow 0$, Choose $\tau, \sigma > 0$

Repeat :

$p \leftarrow Proj_P(p + \sigma(\nabla\bar{u} - \bar{v}))$

$q \leftarrow Proj_Q(q + \sigma\varepsilon\bar{v})$

$u_{old} \leftarrow u$

$u \leftarrow Prox(u + \tau div_1 p)$

$\bar{u} \leftarrow 2u - u_{old}$

$v_{old} \leftarrow v$

$v \leftarrow v + \tau(p + div_2 q)$

$\bar{v} \leftarrow 2v - v_{old}$

Until convergence of u

Return u.

where $Proj_P(p) = \frac{p}{\max\{1, \|p\|/\alpha_1\}}$, $Proj_Q(q) = \frac{q}{\max\{1, \|q\|/\alpha_0\}}$, $Prox(u) = \frac{\lambda u + \tau f}{\lambda + \tau}$.

In Figure 2.2 and Figure 2.3, TGV^2 is applied to a ramp image. While TV (ROF model) causes the significant staircase artifacts and HOTV (LLT model) makes edges blur, TGV^2 yields results that have smooth intensity changes and preserve edges.

2.1.3 Hybrid model

A major challenge that a model using only higher order derivatives faces is to maintain edges in its reconstructions. And it may leave a splotchy artifact in flat regions and produce a speckle artifact on the edges [75] ; see

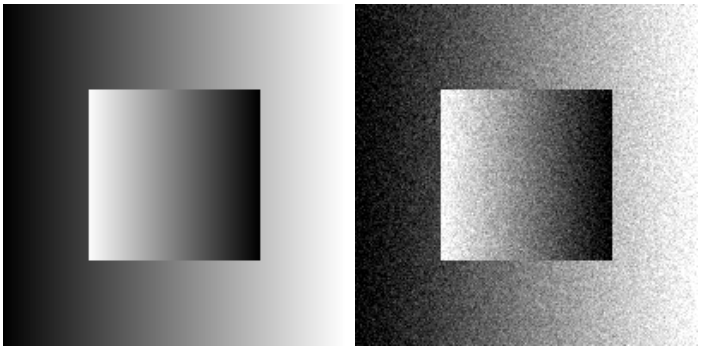

(a) Original (b) Noisy (SNR = 13.47)

Figure 2.2: A ramp image(a piecewise affine artificial image) : the original image consists of regions with vanishing second derivative.

Figure 2.3b Hybrid models that use both lower and higher order derivatives have been proposed to on the one hand, preserve the discontinuities along edges, and on the other, recover smooth regions.

The inf-convolution model [17] is one of the earliest approaches of this type of model. Chambolle et al. [17] solved the inf-convolution problem of two convex regularizers (TV and TV of the gradient). Here, a noisy image is decomposed into three parts $f = u_1 + u_2 + n$, where u_1 is the piecewise constant part, u_2 is the piecewise smooth part, and n is the noise.

$$\min_{u_1,u_2} \int_\Omega |\nabla u_1| + \alpha \int_\Omega |\nabla^2 u_2| + \frac{\mu}{2} \int_\Omega (f - u_1 - u_2)^2 \tag{2.1.11}$$

By minimizing this energy (2.1.11), we can preserve the discontinuous component of the image by u_1, while the regions with smooth intensity transitions are well approximated by u_2. Another approach [45] is to alternately solve the second-order PDE derived from (2.1.2) and the fourth-order PDE derived from (2.1.6). The convex combination of the solutions of (2.1.2) and (2.1.6) can be used to efficiently deal with the discontinuous and smooth regions. In [43] and [55], authors considered a hybrid model that uses an edge detection function $g(x)$ as $g = \frac{1}{1+\|\nabla(G_\sigma * f)\|_2^2}$, where G_σ is the Gaussian kernel with standard deviation σ:

$$\min_u \int_\Omega (1-g)|\nabla u| + g|\nabla^2 u| + \frac{\mu}{2} \int_\Omega (u - f)^2 \tag{2.1.12}$$

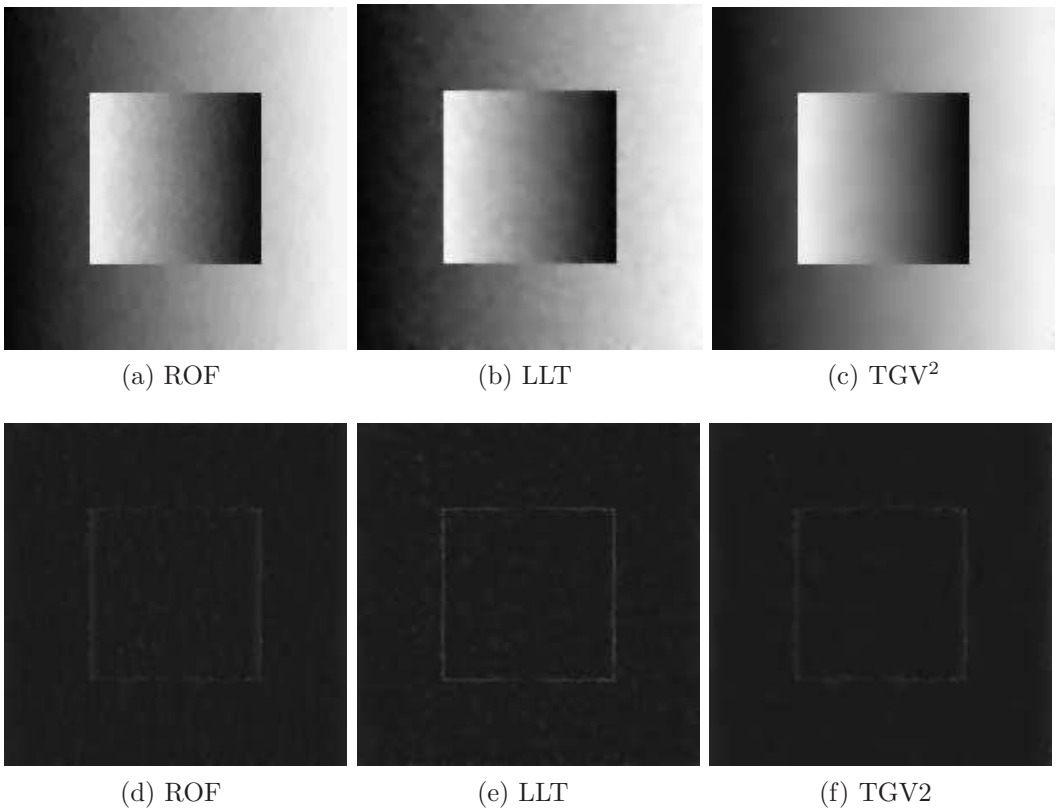

(a) ROF (b) LLT (c) TGV^2

(d) ROF (e) LLT (f) TGV2

Figure 2.3: We compare TGV^2 with the ROF and LLT models. To demonstrate the superiority of TGV^2, we use three different measures; SNR (Signal-to-noise ratio), MRSE (Mean root squared error), MAE (Mean absolute error).

SNR	(a) ROF : 26.21	(b) LLT : 25.12	(c) TGV^2 : 27.24
MRSE	(a) ROF : 0.0155	(b) LLT : 0.0175	(c) TGV^2 : 0.0137
MAE	(a) ROF : 0.0111	(b) LLT : 0.0112	(c) TGV^2 : 0.0080

This model can balance the ROF and LLT models automatically by using the edge detection function g. In [56], authors proved the existence and uniqueness of combined model's minimizers using a relaxation technique in $BV^2(\Omega)$.

2.1.4 Non-convex model

Variational models based on PDE have been successfully applied to noise removal. It is important to choose an appropriate regularizer in the variational framework. In order to study more precisely the influence of the regularization term, we focus on minimizing the following energy functional for image denoising :

$$\min_u E(u) = \int_\Omega \phi(|\nabla u|) + \frac{\mu}{2}\int_\Omega (u-f)^2 \tag{2.1.13}$$

where the first term is the regularization of image u, the second term is the fidelity to the observed image f, μ is a regularization parameter to balance the influence between two terms and ϕ is called a potential function.

As we mentioned in the previous subsection 2.1.1, the idea of regularization was originally introduced by Tikhonov et al. [66], who set $\phi(x) = x^2$. The popular ROF model [59] takes the form $\phi(x) = x$ to preserve edges. Most of these image denoising models are based on convex potential. When a function ϕ is convex and linear at infinity, the existence and uniqueness of a solution of minimization problem (2.1.13) in $BV(\Omega)$ is proved.

To recover and preserve edges in image, it would certainly be preferable to impose a growth condition of the type $\lim_{x\to\infty} \phi(x) = \beta > 0$. In this case, $\phi(|\nabla u|)$ would not penalize strong edges, since it would cost nothing. Unfortunately, since we also want ϕ to have a quadratic behavior near zero, the ϕ should have a non-convex shape. Of course, there is no longer the uniqueness of a solution to the minimization problem. Nevertheless, non-convex potential provides better results than convex potential with linear growth [2].

If the given image f is not a constant, Chipot et al. [28] proved that the functional $E(u)$ with the non-convex potential $\phi(x) = \frac{x^2}{1+x^2}$ has no minimizer in any reasonable space. By the additional spatial constraint, the existence of a minimizer is proved to be satisfied [28].

In spite of the lack of a rigorous mathematical theory for the continuous minimization problem of (2.1.13) with the non-convex potential, its associated discrete version can be solved numerically, such as the gradient decent algorithm [57], the half-quadratic algorithms [2, 22, 64] , the graduated non-convexity (GNC) algorithm [9, 51, 52] and so on.

In [57], Perona and Malik pioneered the anisotropic diffusion (PM diffusion) given by

$$u_t = div(c(x,y;t) \times \nabla u(x,y;t)),\ u_0 = u(x,y;0) \tag{2.1.14}$$

where $c(x,y;t) = \dfrac{1}{1+(\frac{|\nabla u(x,y;t)|}{K_0})^2}$ or $c(x,y;t) = \exp(-\frac{|\nabla u(x,y;t)|}{K_0})^2$ control the rate of diffusion.

The regularization formulations (potential function) corresponding to (2.1.14) are

$$\phi(|\nabla u|) = \frac{K_0^2}{2}\int_\Omega \log(1+(\frac{|\nabla u(x,y;t)|}{K_0})^2)\ d\Omega \tag{2.1.15}$$

$$\phi(|\nabla u|) = \frac{K_0^2}{2}\int_\Omega 1-\exp(-\frac{|\nabla u(x,y;t)|}{K_0})^2\ d\Omega \tag{2.1.16}$$

respectively.

PM diffusion can sharpen edges as well as preserve edges due to the non-convexity of corresponding potential. It is considered as the first model that shows the advantages of the non-convex potential function. We can derive the PM diffusion equation (2.1.14) from (2.1.15) or (2.1.16) by using the gradient decent algorithm.

The half-quadratic algorithm

Now, we consider the half-quadratic algorithm. To compute the solution u of minimization problem (2.1.13) numerically, we can use the half-quadratic algorithm relied on the following duality results.

Theorem 2.1.2 (**[2]**). *Let $\phi : [0,\infty) \to [0,\infty[$ be such that $\phi(\sqrt{s})$ is concave on $]0,\infty[$ and $\phi(s)$ is non-decreasing. Let L and M be defined by $L = \lim_{s\to\infty}\dfrac{\phi'(s)}{2s}$ and $M = \lim_{s\to 0}\dfrac{\phi'(s)}{2s}$. Then there exists a convex and decreasing function $\psi :]L,M] \to [\beta_1,\beta_2]$ such that*

$$\phi(s) = \inf_{L\le b\le M}(bs^2+\psi(b)) \tag{2.1.17}$$

where $\beta_1 = \lim_{s\to 0}\phi(s)$ and $\beta_2 = \lim_{s\to\infty}(\phi(s)-\dfrac{s\phi'(s)}{2})$. Moreover, for every $s \ge 0$, the value b for which the minimum is reached is given by $b = \frac{\phi'(s)}{2s}$. The additional variable b is usually called the dual variable.

Table 2.1: Examples of function ϕ

Name of the function $\phi(s)$	$\phi(s)$	convexity	$\psi(s)$	$\frac{\phi'(s)}{2s}$
Hyper surfaces	$2\sqrt{1+s^2}-2$	YES	$b+\frac{1}{b}$	$\frac{1}{\sqrt{1+s^2}}$
Hebert and Leahy	$\log(1+s^2)$	NO	$b-\log(b)-1$	$\frac{1}{1+s^2}$
Geman and McClure	$\frac{s^2}{1+s^2}$	NO	$b-\sqrt{b}+1$	$\frac{1}{(1+s^2)^2}$

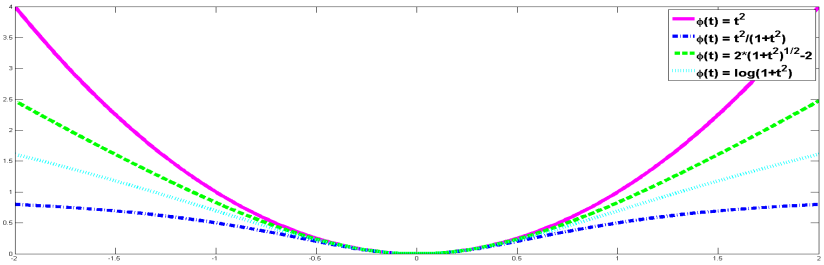

(a) Potential functions 1

Figure 2.4: $\phi(t) = 2\sqrt{1+t^2}-2$, $\log(1+t^2)$, $\frac{t^2}{1+t^2}$

The main idea of this algorithm is to introduce an auxiliary variable b and construct an augmented criterion $J(u,b)$, which is quadratic in u and separable in b.

We can consider three examples of function ϕ : $\phi(t) = 2\sqrt{1+t^2}-2$, $\log(1+t^2)$, $\frac{t^2}{1+t^2}$. Table 2.1 and Figure 2.4 show three potential functions and corresponding functions ψ [2, 64].

The half-quadratic algorithm only assumes that $\phi(\sqrt{x})$ is concave, thus it can be applied to convex and non-convex potentials ϕ. But in all cases, the function ψ in (2.1.17) is always convex. Of course, there is no convergence results for the non-convex potential.

Now we present how to apply Theorem 2.1.2 to solving the problem (2.1.13), where $\phi(s) = \frac{\alpha s^2}{1+\alpha s^2}$ is non-convex.

$$E(u) = \int \frac{\alpha|\nabla u|^2}{1+\alpha|\nabla u|^2} + \frac{\mu}{2}\|u-f\|_2^2$$

Since $\phi(s)$ satisfies the hypotheses of Theorem 2.1.2, there exist L, M and ψ such that

$$E(u) = \int \inf_{L \le b \le M} (b|\nabla u|^2 + \psi(b)) + \frac{\mu}{2}\|u - f\|_2^2$$

Since we convert the infimum with respect to u and b, we can get the following functional

$$\begin{aligned} \inf_u \ E(u) &= \inf_u \inf_b \{ \int (b|\nabla u|^2 + \psi(b)) + \frac{\mu}{2}\|u - f\|_2^2 \} \\ &= \inf_b \inf_u \{ \int (b|\nabla u|^2 + \psi(b)) + \frac{\mu}{2}\|u - f\|_2^2 \} \\ &= J(u, b) \end{aligned} \tag{2.1.18}$$

where $\psi(b) = (\frac{b}{\sqrt{\alpha}} - 1)^2,\ b = \frac{\phi'(s)}{2s} = \frac{\alpha}{(1 + \alpha s^2)^2}$.

$J(u, b)$ is convex both in u and in b, but it is not convex in the pair (u, b). So we can derive alternative minimization algorithm as follows :

Algorithm 2: The half-quadratic algorithm

step 1 : $u^{n+1} = \arg\min_u J(u, b^n) = \arg\min_u \int b^n|\nabla u|^2 + \frac{\mu}{2}\|u - f\|_2^2$

$\rightarrow (2b^n \nabla^\top \nabla + \mu)u = \mu f$

step 2 : $b^{n+1} = \arg\min_b J(u^{n+1}, b) = \arg\min_b \int b|\nabla u^{n+1}|^2 + \psi(b)$

$\rightarrow b = \frac{\phi'(|\nabla u^{n+1}|)}{2|\nabla u^{n+1}|} = \frac{\alpha}{(1 + \alpha|\nabla u^{n+1}|^2)^2}$

Go back to the first step until there is convergence.

The above linear system in step 1 can be solved by a Gauss-Seidel iterative method. Under the periodic boundary condition of u, the linear system can be efficiently solved by using fast fourier transform (FFT). If we assume the reflexive boundary condition of u, we can adopt discrete cosine transform (DCT) [14, 49, 50] instead of FFT. In Figure 2.5, numerical result is displayed. We use the half-quadratic algorithm for a non-convex potential function $\phi(t) = \frac{\alpha|t|^2}{1+\alpha|t|^2}$.

Remark : The relation between Geman-McClure function and Mumford-shah energy.

As we mentioned, using the non-convex Geman-McClure function as a regularizer yields the non-existence of a minimizer of the problem, that is

(a) Noisy (b) $\phi(t) = \frac{\alpha|t|^2}{1+\alpha|t|^2}$ (c) Dual variable b

Figure 2.5: Restoration parameters :$\alpha = 20; \mu = 60$; (a) Noisy image, SNR $= 11.41$ (b) Denoised image, SNR $= 16.63$ (c) the dual variable b

proved in [28]. Authors proved the existence of a minimizer by using the Geman-McClure function with an additional spatial edge organization constraint. It is actually equivalent to approximated Mumford-shah functional using $\Gamma-$convergence framework [7, 64].

Non-smooth graduated non-convexity (GNC) algorithm

Recently, Nikolova et al. [51, 52] have proposed to track a sequence of approximate non-smooth energy functions with non-smooth and the non-convex potential in image restoration.

In [52], authors dealt with non-convex non-smooth minimization methods for image restoration and reconstruction

$$\min_u E(u) = \|Ku - f\|_2^2 + \beta \sum_{i \in I} \phi(\|D_i u\|_2) \tag{2.1.19}$$

To reveal the essential properties of minimizers of E, we present assumptions to the potential ϕ as follows:

- H1 : $Ker(K) \cap Ker(D) = 0$, where $D = [D_1^\top, \cdots, D_p^\top]^\top$
- H2 : ϕ is continuous and symmetric on $\mathbb{R}$, increasing on $\mathbb{R}_+$, with $\phi(0) = 0$ and $\phi'(0^+) > 0$

- H3 : ϕ is $\mathcal{C}^2$ on $\mathbb{R}_+^* \setminus M$ where $0 \notin M$ is a finite set of points s.t. if $t \in M$ then $\phi'(t^-) > \phi'(t^+)$ and $-\infty < \ddot{\phi}(t^-) := \lim_{\tau \nearrow t} \phi''(t) < \ddot{\phi}(t^+) := \lim_{\tau \searrow t} \phi''(t) \leq 0$
- H4 : $\ddot{\phi}(0^+) := \lim_{t \nearrow 0} \phi''(t) < 0, \phi''$ is increasing with $\phi''(t) \leq 0 \; \forall t \in \mathbb{R}_+^* \setminus M$ and $\lim_{t \to \infty} \phi''(t) = 0$

There are potential functions yielding non-smooth and non-convex regularization and satisfying H2, H3 and H4 : $t^\alpha, \alpha \in (0,1)$; $\frac{\alpha t}{1+\alpha t}$; $\log(\alpha t + 1); \cdots$ Under the above assumptions, they showed that the solution of the non-convex non-smooth minimization problem is composed of constant regions surrounded by closed contours and neat edges.

Theorem 2.1.3 ([**52**])**.** *Let E be of the form (2.1.19) for $\beta > 0$, and all assumptions H1,H2,H3, and H4 hold. Given $f \in \mathbb{R}^q$, let $\hat{u}$ be any (local) minimizer of E. Then we have*

$$\text{either } \|D_i \hat{u}\|_2 = 0 \text{ or } \|D_i \hat{u}\|_2 \geq \theta, \qquad \forall i \in I \tag{2.1.20}$$

where $0 < \theta < T$.

In other words, if $\{D_i\}$ are discrete gradients, the minimizers $\hat{u}$ are composed of constant regions surrounded by closed contours and neat edges higher than a bound $\theta > 0$. The solution is then a segmented image, for any operator K.

The main goal of this work [52] is to develop fast minimization algorithms to solve the non-convex non-smooth minimization problem. Since the given minimization problem is non-convex, there may be a large number of local minima ; see Figure 2.6. Usual gradient-based methods are inappropriate due to its non-smoothness and the matrix K is often ill-conditioned. They followed a non-smooth graduated non-convexity (GNC) approach. The GNC approach tracks a sequence of approximations of the energy E.

In Figure 2.6 [9], the strategy of the GNC method for finding the solution is illustrated. In this case, a sequence of just 4 functionals $\{E_0, E_{1/3}, E_{2/3}, E_1\}$ is used to optimize the non-convex functional E. A non-convex functional

$E = E_1$ is approximated by a convex functional $E^* = E_0$. Initially. a minimizer of E_0 may not be a global minimizer of $E = E_1$. But, successive minimization of sequences E_ϵ, as ϵ increases run downhill to reach the true global optimum of $E = E_1$.

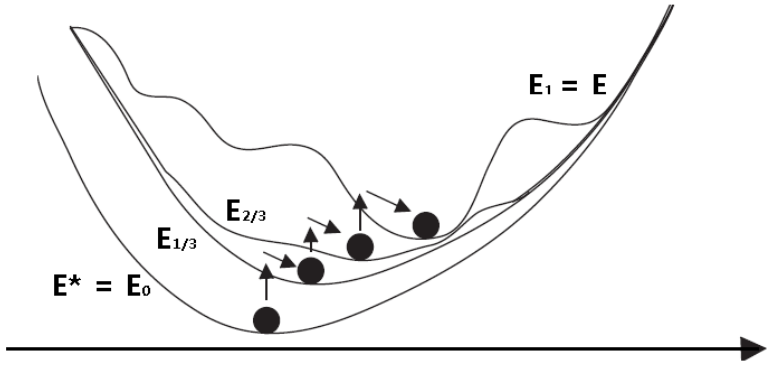

Figure 2.6: The illustration of the GNC method.

Similarly, a non-smooth GNC continuation method is inaugurated to solve a non-convex non-smooth minimization problem.

First, consider a sequence

$$\epsilon_0 = 0 < \epsilon_1 < \cdots < \epsilon_p < \cdots < \epsilon_n = 1$$

Let $\phi_{\epsilon_0} = \phi_0$ be convex and a sequence ϕ_{ϵ_p} monotonously reaches ϕ as $\epsilon_p : 0 \to 1$, with $\phi_{\epsilon_n} = \phi_1 = \phi$. So, the following energy sequence E_{ϵ_p} approximate our energy E.

$$E_{\epsilon_p}(u) = \|Ku - f\|_2^2 + \beta \sum_{i \in I} \phi_{\epsilon_p}(\|D_i u\|_2), \qquad \text{where } 0 \le \epsilon_p \le 1$$

How to choose the approximating sequence ϕ_{ϵ_p} is important for the GNC continuation method. For the computational reasons, there are additional assumptions as follows:

- H5: $\phi'(0^+) > 0$ and $\lim_{t \nearrow 0} \phi''(t) < 0$ are finite.
- H6: The set M is empty.

From all hypotheses that we assume, we can choose

$$\phi_{\epsilon_p}(t) = \psi_{\epsilon_p}(t) + \alpha_{\epsilon_p}|t| \quad \text{where} \quad \alpha_{\epsilon_p} = \phi'_{\epsilon_p}(0^+) \tag{2.1.21}$$

that is split into a non-smooth regularization term and the TV type regularization term. Finally, we can yield the below formulation

$$\min_u E_{\epsilon_p}(u) = \|Ku - f\|_2^2 + \beta\Psi_{\epsilon_p}(u) + \beta\alpha_{\epsilon_p}\sum_{i\in I}\|D_i u\|_2 \tag{2.1.22}$$

where $\Psi_{\epsilon_p}(u) = \sum_{i\in I}\psi_{\epsilon_p}(\|D_i u\|_2)$.

Based upon the decomposition of (2.1.21), variable-splitting and penalty techniques are applied to address the difficulties for minimizing the energy E_{ϵ_p} (2.1.22). Nikolova et al. developed two fast numerical schemes as follows:

1. Numerical scheme based upon fitting to u
   $E_{\epsilon_p}(u, v) = \|Ku - f\|_2^2 + \beta\Psi_{\epsilon_p}(u) + \beta\alpha_{\epsilon_p}TV(v) + \omega\|u - v\|_2^2$

2. Numerical scheme based upon fitting to Du
   $E_{\epsilon_p}(u, v) = \|Ku - f\|_2^2 + \beta\Psi_{\epsilon_p}(u) + \omega\|Du - v\|_2^2 + \beta\alpha_{\epsilon_p}\sum_{i\in I}\|v_i\|_2$

Authors solve it alternately, first minimize $v^{(j,p)}$ by using simple shrinkage and then minimize $u^{(j,p)}$ by the Quasi-Newton method.

We consider the non-convex potential functions: see Figure 2.7. $\phi(t) = \frac{\alpha|t|}{1+\alpha|t|}$, $\phi_\epsilon(t) = \frac{\alpha|t|}{1+\epsilon\alpha|t|}$, $0 \le \epsilon \le 1$.

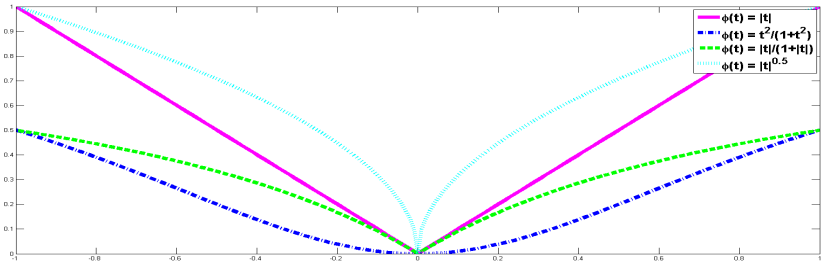

(a) Potential functions 2

Figure 2.7: $\phi(t) = \frac{t^2}{1+t^2}, \frac{\alpha|t|}{1+\alpha|t|}, |t|^\alpha$

(a) Original (b) Noisy (c) ROF

(d) $\phi(t) = |t|^{0.8}$ (e) $\phi(t) = \frac{0.5|t|}{1+0.5|t|}$ (f) $\phi(t) = \frac{0.5|t|}{1+0.5|t|}$

Figure 2.8: Restoration parameters :$\alpha_\epsilon = 0.5; \beta = 0.65$; (a) Original image (b) Noisy, SNR=2.52 (c) SNR=11.29 (d) SNR=11.54 (e) Numerical scheme based upon fitting to u, SNR=11.49 (f) Numerical scheme based upon fitting to Du, SNR = 10.57

In Figure 2.8, the numerical experiments show that non-convex potential provides better results than convex potential for piecewise constant image.

Non-convex TV

A non-convex model with anisotropic TV [39] was proposed on the basis of the statistical observation that natural image gradients have a heavy-tailed distribution. Note that such distribution provides a natural prior for image denoising, and such a prior is called a sparse prior. In [41] and [42], the authors assert that the Gaussian prior distributes the image gradient

(a) Lena image

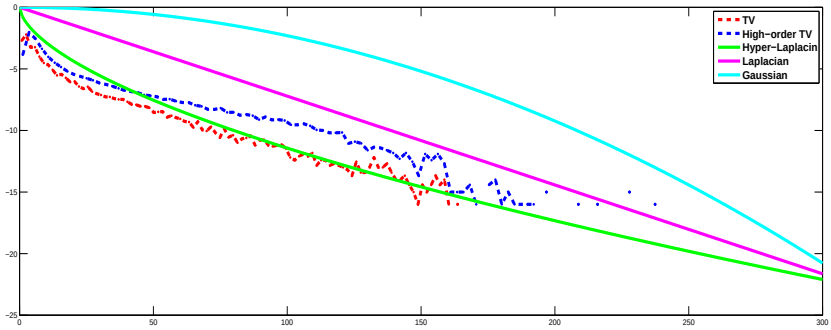

(b) The distributions of TV($\|\nabla u\|_2$) and higher order TV($\|\nabla^2 u\|_2$).

Figure 2.9: Two curves are below the straight line. It means that these distributions of $\|\nabla u\|_2$ and $\|\nabla^2 u\|_2$ are sparse.

magnitude equally in the entire image domain, while the spare prior makes the image gradient magnitude zero in the entire image domain except for the edges and dominant features. This produces sharper edges, reduces noises and helps remove image artifacts. Therefore, this property is under intensive research [33, 60, 39]. In particular, these distributions have been modeled by a hyper-Laplacian, $p(x) \propto e^{-k|x|^\alpha}$ with $0.5 \leq \alpha \leq 0.8$ [39]. In other words, their distribution are fitted into not Laplacian($\|\cdot\|_2^1$) and Gaussian($\|\cdot\|_2^2$) but hyper-Laplacian: see Figure 2.9.

The efficient method based on the penalty approximation to solve non-convex hyper-Laplacian priors was proposed for two specific values of $\alpha = \frac{1}{2}, \frac{2}{3}$. In [67], authors used non-convex multi-resolution derivative filters as a regularizer with multistage convex relaxation [77]. There are non-convex

variational models using TV^q $(0 \leq q \leq 1)$ [35].

$$\min_{u \in H_0^1(\Omega)} \int_\Omega (\frac{\mu}{2}|\nabla^2 u|^2 + \frac{\alpha}{q}|\nabla u|^q + \frac{\lambda}{2}|Ku - f|^2)dx \tag{2.1.23}$$

where $\alpha > 0, 0 < \mu \ll \alpha, f \in L^2(\Omega), \lambda \in L^\infty(\Omega)$ such that $\lambda(x) > 0$ a.e on Ω and $\int_\Omega \lambda(x)dx = Area(\Omega)$ and $K \in \mathcal{L}(L^2(\Omega))$. Hintermüller et al. [35] studied to minimize the support of the gradient of the recovered images and introduced TV^q model to keep the edge-preserving property and promote gradient-sparsity. Chartrand [23] has also shown that a non-convex penalty term $(\int_\Omega |\nabla u|^\alpha, 0 < \alpha < 1)$ is better able to preserve shapes. Even though TV penalizes the length of object edges, the non-convex regularization only penalizes the boundaries of dimension at least $2-\alpha$. Thus, it will not penalize most shapes at all.

Such researches on the higher order model, hybrid models and non-convex regularizers has motivated us to develop a new variational model that uses a convex combination of the non-convex TV $(\|\nabla u\|_2^\alpha, \alpha < 1)$ and the non-convex HOTV $(\|\nabla^2 u\|_2^\alpha, \alpha < 1)$ for the image denoising problem. In the following chapter 3, we will deal with this subject in detail.

Although the non-convex variational model with the anisotropic TV has been studied previously, to the best of our knowledge, no research has been conducted on the non-convex variational model with HOTV thus far. This is the main contribution of the following chapter 3.

2.2 Image decomposition

We aim to separate an image f into two components u and v, where u holds geometric components or structural information and v holds the oscillatory or textured components. Before considering the image decomposition problem in variation approaches, we have a fundamental question : what is the benefit in image decomposition to cartoon and texture? There are applications that may benefit from such decomposition. For example, there are edge detection in textured image, image inpainting, object recognition and so on.

There are many image decomposition model based on TV regularization. In terms of images, images are discontinuous across edges. So, the space of functions of bounded variation (BV(Ω)) is the function space that is commonly used in image analysis. In TV minimization framework, we can decompose a given image into a sum of two function $u+v$, where u is a function of BV, while v is a function representing the texture or noise. To model v, we use the space of oscillating functions, which is in some sense the dual of the BV space.

2.2.1 Meyer's model

Meyer [48] also chose BV space to recover the image u, but he proposed the new spaces which better model oscillatory components v. Let us begin with a definition.

Definition 2.2.1 ([**48**])**.** Let G denote the Banach space consisting of all generalized functions $f(x)$ which can be written as

$$f(x) = \partial_1 g_1(x) + \partial_2 g_2(x) = div(g(x)), \qquad g_1, g_2 \in L^\infty(R^2)$$

$$\|f\|_G = \inf_g \quad \{ \quad \|g\|_\infty | f = div(g),\ g = (g_1, g_2),\ g_1, g_2 \in L^\infty,$$
$$\|g(x)\| = \sqrt{|g_1|^2 + |g_2|^2}(x)\ \}$$

In other words, the ROF model has been generalized to use the weaker norms, G, as a penalty term, instead of the $\|\cdot\|^2_{L^2(\Omega)}$

$$\inf_{(u,v)\in BV\times G / f=u+v} \{ \int |\nabla u| + \lambda \|v\|_G \} \tag{2.2.1}$$

Related works have been proposed in [54, 4, 6], where authors approximated Meyer's model. Motivated by the fact G = $\dot{W}^{-1,\infty}$, Osher et al. [54] proposed TV-H^{-1} model by introducing $H^{-1} = \dot{W}^{-1,2}$ norm to approximate the G-norm. In [4, 6], authors have considered Hilbert spaces to model oscillatory patterns. Hilbert spaces $\mathcal{H}$ are defined thank to a linear symmetric positive operator K with $< f, g >_{\mathcal{H}} = < f, Kg >_{L^2}$.

$$\inf_{(u,v)\in BV\times \mathcal{H} / f=u+v} \{ \int |\nabla u| + \lambda \|v\|^2_{\mathcal{H}} \} \tag{2.2.2}$$

where $\|v\|_{\mathcal{H}}^2 =< v, v >_{\mathcal{H}} =< v, Kv >_{L^2} = \|\sqrt{K}v\|_{L^2}^2$. Especially, when $\mathcal{H} = H^{-1} = (H_0^1)^*$, K becomes $-\Delta^{-1}$ and we can obtain TV-H^{-1} model

$$\inf_{(u,v)}\{\int |\nabla u| + \lambda\|v\|_{H^{-1}}^2\} = \inf_{(u,v)}\{\int |\nabla u| + \int |\nabla\Delta^{-1}v|^2 dx\} \tag{2.2.3}$$

TV-Hilbert model is the generalized version of TV-H^{-1} model. Another variant of the Meyer's model is the A^2BC model [3] which is solved by the Chambolle's projection algorithm [16].

2.2.2 Nonlinear filter

To decompose an image into base and texture components, there is a very rich literature on image filtering based techniques. We start with linear filters, such as smoothing with averaging, smoothing with Gaussian. These filters are simple and easy to implement. However they may smooth not only oscillating patterns but also structural information. Thus, linear filtering based techniques cannot make a clear decomposition between cartoon and textures.

It's led to numerous research to develop the edge-preserving smoothing operator, resulting in non-linear filters such as anisotropic diffusion [57, 72], bilateral filter [68], trilateral filter [29], weighted least squares(WLS) filter [32] etc. The bilateral filter proposed by Tomasi et al. [68] is so popular and has its various variants and extensions.

$$\begin{aligned} BLF(f,\sigma_s,\sigma_r) &= \frac{1}{C(x)}\int f(y)e^{-\frac{1}{2}(\frac{|y-x|}{\sigma_s})^2}e^{-\frac{1}{2}(\frac{|f(y)-f(x)|}{\sigma_r})^2}dy \\ \text{where} \quad C(x) &= \int e^{-\frac{1}{2}(\frac{|y-x|}{\sigma_s})^2}e^{-\frac{1}{2}(\frac{|f(y)-f(x)|}{\sigma_r})^2}dy \end{aligned} \tag{2.2.4}$$

Each pixel in the filtered image is the weighted average of its neighbors, with the weight decreasing both with spatial distance and with distance in intensity value. Hence, it behaves like weighted heat equation, enhancing the edge. Recently, WLS filter is proposed by Farbman et al. [32], which captures details at a variety of scales. It is formulated as follows

$$\begin{aligned} \min_u \quad & (u-f)^2 + \lambda(a_x(f)(\nabla_x u)^2 + a_y(f)(\nabla_y u)^2) \\ \text{where} \quad & a_x(f) = (|\nabla_x f|^\alpha + \epsilon)^{-1}, a_y(f) = (|\nabla_y f|^\alpha + \epsilon)^{-1} \end{aligned} \tag{2.2.5}$$

Finally, u is obtained from f by applying a nonlinear operator F_λ.

$$u = F_\lambda(f) = (I + \lambda L_f)^{-1}(f) \text{ where } L_f = (D_x)^\top A_x D_x + (D_y)^\top A_y D_y$$

These filters are quite effective at smoothing small changes in intensity value while preserving strong edges. But both of them are unable to distinguish between high-contrast texture and similar contrast edges.

In [13], Buades et al. proposed a fast approximate solution to the original variational problem. The algorithm proceeds as follows.

- To decide whether each point belongs to the cartoon part or to the textural part,

  1. compute a local total variation of the image around the point.
  2. convolve these moduli with the Gaussian G_σ to get the local total variation of f and $L_\sigma * f$
  3. deduce the value of the relative reduction of LTV $\lambda_\sigma(x)$ at each point in the image.

  A point which has a slowly varying local total variation is considered as a point that belongs to structure components. However, textural points show a strong decay of their local total variation. The cartoon+texture filter pair is based on this simple observation.

- The cartoon part must keep the original image values f at points . At points identified as texture points, the cartoon part takes the filtered value $g = L_\sigma * f$. A fast nonlinear low pass and high pass filter pair can be computed by doing weighted averages of f and $g = L_\sigma * f$ depending on the relative reduction of LTV λ_σ. The weight $w(x) : [0, 1] \to [0, 1]$ is a nondecreasing piecewise affine function displayed in Figure 2.10.

- Compute the texture v as the difference $u - f$.

The above algorithm are simply formulated as

$$\begin{aligned} u(x) &= w(\lambda_\sigma(x))(L_\sigma * f)(x) + (1 - w(\lambda_\sigma(x)))f(x) \\ v(x) &= f(x) - u(x) \end{aligned}$$

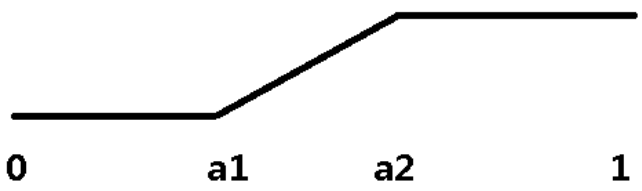

Figure 2.10: The soft threshold function $w(s)$

This non-linear filter, called BLMV filter, is as simple and rapid as a linear filter while keeping the essential features of Meyer's model. In Figure 2.11, decomposition results by the bilateral filter, WLF filter, BLMV filter are displayed.

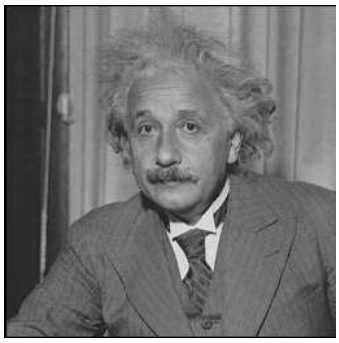

(a) Original

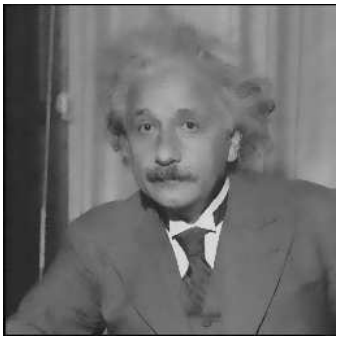

(b) Bilateral filter u

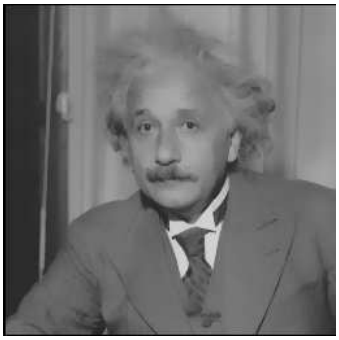

(c) WLS filter u

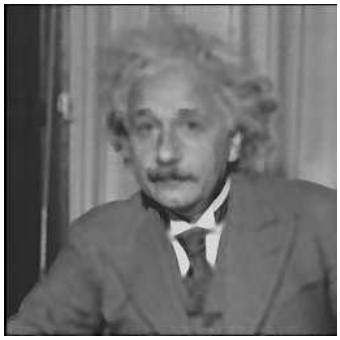

(d) BLMV filter u

(e) Bilateral filter v

(f) WLS filter v

(g) BLMV filter v

Figure 2.11: Decomposition results by the bilateral filter, WLF filter, BLMV filter. (a) Original image (b) Bilateral filter u ($N = 3, \sigma_s = 3, \sigma_r = 0.1$) (c) WLS filter u ($\lambda = 0.125, \alpha = 1.2$) (d) BLMV filter u ($\sigma = 2.5$) (e) Bilateral filter v (f) WLS filter v (g) BLMV filter v

Chapter 3

Non-convex hybrid TV for image denoising

Image restoration problems, such as image denoising, are important steps in various image processing method, such as image segmentation and object recognition. Due to the edge preserving property of the convex TV, variational model with TV is commonly used in image restoration. However, staircase artifacts are frequently observed in restored smoothed region. To remove the staircase artifacts in smoothed region, convex HOTV regularization methods are introduced. But the valuable edge information of the image is also attenuated. In this chapter, we propose non-convex hybrid TV regularization method to significantly reduce staircase artifacts while well preserving the valuable edge information of the image. To efficiently find a solution of the variation model with the proposed regularizer, we use the iterative reweighted method with the augmented Lagrangian based algorithm. The proposed model shows the best performance in terms of the SNR and the structure similarity index measure (SSIM) with comparable computational complexity.

Notation

Hereafter, we will restrict our attention to the discrete setting. We assume that the gray image region Ω is an $N \times N$ matrix and set $R^{N\times N} = V, V \times V = Q$ and $V^{2\times 2} = Z$. For $u \in V$, ∇u is given by $(\nabla u)_{i,j} = ((D_x^+ u)_{i,j}, (D_y^+ u)_{i,j}) \in Q$. $D_x^+ u$ and $D_y^+ u$ denote the first-order forward difference operators with the

reflexive boundary condition:

$$(D_x^+u)_{i,j}=\begin{cases} u_{i,j+1}-u_{i,j} & 1\le j<N \\ 0 & j=N \end{cases}, (D_y^+u)_{i,j}=\begin{cases} u_{i+1,j}-u_{i,j} & 1\le i<N \\ 0 & i=N \end{cases}$$

We also denote the first-order backward difference operators as D_x^-u and D_y^-u with the reflexive boundary condition:

$$(D_x^-u)_{i,j}=\begin{cases} 0 & j=1 \\ u_{i,j}-u_{i,j-1} & 1<j\le N \end{cases}, (D_y^-u)_{i,j}=\begin{cases} 0 & i=1 \\ u_{i,j}-u_{i-1,j} & 1<i\le N \end{cases}$$

On the basis of the above operators, we can obtain the second-order difference operator as

$$(\nabla^2u)_{i,j}=\begin{pmatrix} D_x^-(D_x^+u)_{i,j} & D_x^+(D_y^+u)_{i,j} \\ D_y^-(D_x^-u)_{i,j} & D_y^-(D_y^+u)_{i,j} \end{pmatrix}\in Z.$$

Finally, we denote the first-order and the second-order divergence operators respectively as

$$(\mathrm{div}u)_{i,j}=(D_x^-u)_{i,j}+(D_y^-u)_{i,j}$$
$$(\mathrm{div}^2u)_{i,j}=D_x^+(D_x^-u)_{i,j}+D_x^-(D_y^-u)_{i,j}+D_y^+(D_x^+u)_{i,j}+D_y^+(D_y^-u)_{i,j}$$

and the adjoint operator of ∇ as $\nabla^\top=-\mathrm{div}$ [73].

3.1 Variational model with non-convex hybrid TV

In this section, we propose a novel variational model with the non-convex hybrid TV regularizer. Before we present our variational model, we introduce two non-convex models.

3.1.1 Non-convex TV model and non-convex HOTV model

First, we consider a model that substitutes $\|\nabla u\|_2^\alpha$ for a regularizer in the ROF model. This model is called the non-convex TV model. This model

minimizes the support of image gradient and yields a piecewise constant solution, as is done by the ROF model. Hence this model works effectively for an image containing mainly piecewise constant regions and sharp edges. However it can lead to staircase effects when applied to a wide range of images that include smooth transition regions instead of being dominated by piecewise constant regions. Contrary to our expectations based on statistical distribution, a non-convex TV regularizer may produce inferior quality to convex TV when applied to images that possess linear regions with non-zero slope. This is demonstrated in detail by the numerical results in section 3.3.

As mentioned in Introduction, HOTV has attracted the attention of researchers only recently [8, 12, 40, 76, 79, 81]. These studies have suggested that HOTV is more suitable for a relatively wide range of image types to produce piecewise linear solutions. In [40], the term $\int_\Omega |\nabla^2 u|$ was justified as an appropriate higher order extension of TV, which proved that it can result in relatively good image restoration with smooth intensity changes, such as for biomedical images, as well as inherit the attractive properties of TV such as convexity and rotation invariance. This research led us to choose $\|\nabla^2 u\|_2$ as the higher order extension of TV among several available choices. Inspired by the above observations, we attempt to introduce the non-convexity of HOTV instead of TV.

We replace the HOTV regularizer of the LLT model with $\|\nabla^2 u\|_2^\alpha$ to minimize the support of HOTV.

$$\min_u \|\nabla^2 u\|_2^\alpha + \frac{\mu}{2}\|u - f\|_2^2 \qquad (\alpha < 1) \tag{3.1.1}$$

We call the modified model the non-convex HOTV model. Even though non-convexity increases the difficulty in analyzing and numerically solving the model, it yields better results than those obtained by convex models such as the ROF and LLT models. Our numerical experiments confirmed that the non-convex HOTV model can achieve a higher SNR value than the LLT model as well as the ROF model. However, the drawback of the non-convex HOTV is that it can blur edges. Numerical results and a detailed explanation are discussed in section 3.3.

3.1.2 The Proposed model: Non-convex hybrid TV model

In order to overcome this drawback described in subsection 3.1.1, the hybrid model was studied further in [43, 45, 55, 56]. One study combined a TV regularizer and an HOTV regularizer convexly [45] and another combined them with an edge detection function as weights [43, 55]. These combinations of TV and HOTV for a regularizer could balance the preservation of edges and smoothness within homogeneous regions in an image. Note that Papafitsoros et al. [56] proposed the following combined first- and second-order variational model.

$$\min_u \frac{1}{2}\int_\Omega (u_0 - T(u))^2 dx + \alpha \int_\Omega f(\nabla u)dx + \beta \int_\Omega g(\nabla^2 u)dx \qquad (3.1.2)$$

where α, β are non-negative regularization parameters, $f : R^2 \to R^+, g : R^4 \to R^+$ are convex functions, and T is a linear operator. They proved the existence and uniqueness of the minimizer using a relaxation technique.

Hereafter, we will consider only the non-convex versions, that is, we propose only the non-convex hybrid TV model for the image denoising problem. To maximize the benefits of non-convex TV and HOTV regularizers and to overcome their weakness, we consider a suitable combination of the two regularizers as for the convex case. We call the resulting model a non-convex hybrid TV model.

Figure 3.1 shows the significance of using the non-convex HOTV and the effect of combining the non-convex TV and the non-convex HOTV. Carefully comparing Figure 3.1d and Figure 3.1e, we can confirm that the non-convex HOTV model deals with piecewise smooth intervals better than the LLT model. The combination of the non-convex TV and the non-convex HOTV reduces the staircase artifacts in smooth transition intervals and simultaneously preserves edges.

One type of the combination is convex [45].

$$\begin{aligned} \min_u \quad & (1-g)\|\nabla u\|_2^{\alpha_1} + g\|\nabla^2 u\|_2^{\alpha_2} + \frac{\mu}{2}\|u - f\|_2^2 \qquad (3.1.3) \\ \text{where} \quad & 0 \le g(=\text{constant}) \le 1 \end{aligned}$$

The regularizer term in the above model corresponds to the non-convex TV and the non-convex HOTV when $g = 0$ and $g = 1$, respectively. Hence, this

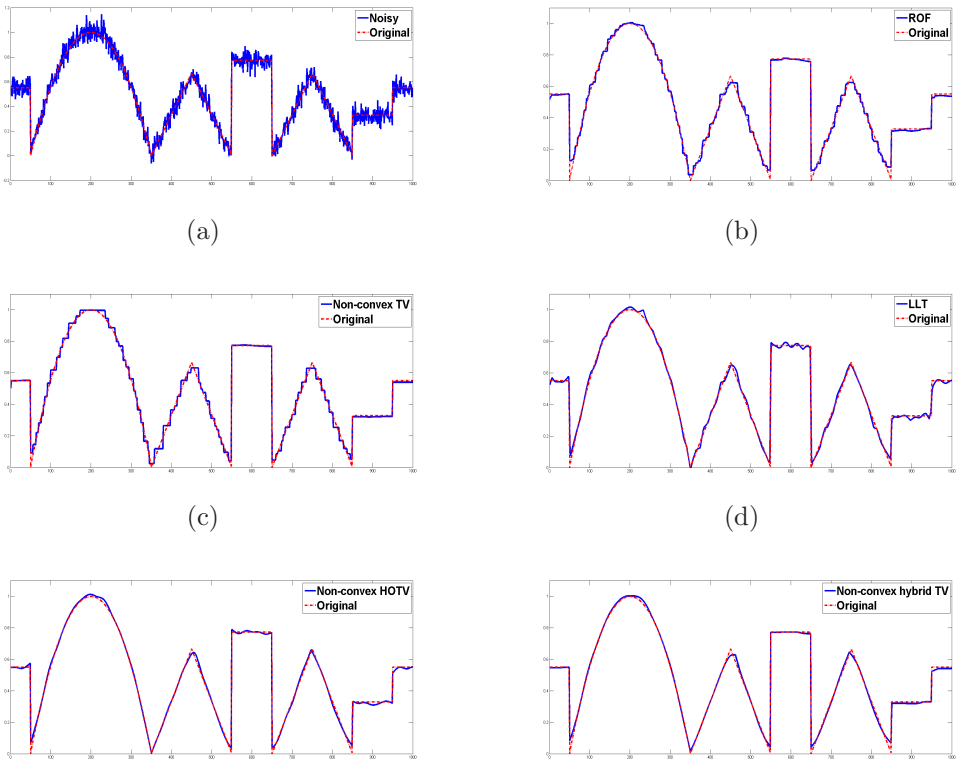

Figure 3.1: Significance of using non-convex HOTV and the effect of combining non-convex TV and non-convex HOTV (1D signal). The non-convex hybrid TV reduces the staircase artifacts in smooth transition intervals and simultaneously preserves edges. (a) Noisy (b) ROF (c) Non-convex TV (d) LLT (e) Non-convex HOTV (f) Non-convex hybrid TV

model balances the non-convex TV and the non-convex HOTV. Second, we adopt the approach proposed by Li et al. [43]:

$$\min_{u} \quad (1-g)\|\nabla u\|_2^{\alpha_1} + g\|\nabla^2 u\|_2^{\alpha_2} + \frac{\mu}{2}\|u-f\|_2^2 \tag{3.1.4}$$

$$\text{where} \quad g(x) = \frac{1}{1+\|\nabla(G_\sigma(x) * f)\|_2^2} \text{ is an edge detection function}$$

The edge detection function can describe the information of edges to au-

tomatically control the regularizer. Next, we minimize the models (3.1.3) and (3.1.4) by using an iterative reweighted algorithm described in the next section.

3.2 Iterative reweighted hybrid Total Variation algorithm

Many algorithms have been developed to solve recovery problems in compressive sensing (CS) [30]. Three main directions emerge: iterative greedy algorithms [46], convex L_1 relaxation [65] and non-convex L_p regularization with $0 < p < 1$ [24, 25]. To measure the sparsity of entries, L_p-norm regularization with $0 < p < 1$ was proposed in the framework of CS instead of L_0- and L_1-norm regularization [15, 26]. The iterative reweighted L_1 minimization (IRL1) method [15, 27] and the iterative reweighted least squares (IRLS) algorithm [26] was developed to minimize the non-convex optimization problems such as the linearly constrained L_p-norm problem and the L_p-norm regularized linear least squares problem.

Similar to the above approaches, we consider adopting iterative reweighted algorithm to solve the non-convex hybrid TV models (3.1.3) and (3.1.4). We call this algorithm the iterative reweighted hybrid TV (IRHTV) algorithm. At each iteration, IRHTV minimizes the convex approximation of (3.1.3) and (3.1.4):

$$u^{k+1} = (1-g)\nu_1(\nabla u^k)\|\nabla u\|_2 + g\nu_2(\nabla^2 u^k)\|\nabla^2 u\|_2 + \frac{\mu}{2}\|u - f\|_2^2 \quad (3.2.1)$$

$$\text{where} \qquad \nu_1(\nabla u^k) = \frac{1}{\|\nabla u^k\|_2^{1-\alpha_1}},\ \nu_2(\nabla^2 u^k) = \frac{1}{\|\nabla^2 u^k\|_2^{1-\alpha_2}}$$

The weight is determined by the solution of the previous iteration. This algorithm is an extension of the lagged diffusivity fixed-point algorithm [69], which is equivalent to the IRLS applied to TV.

IRHTV is composed of two main steps, weight update followed by image update in which (3.2.1) is minimized.

As shown in Algorithm 1, we replace $\|\nabla^i u^{n-1}\|_2^{\alpha_i-1}, i=1,2$ with $\|\nabla^i u^{n-1}+\eta\|_2^{\alpha_i-1}$ in the weight update step to prevent weights from involving division by zero. And we set $\eta=1.e-5$ in all experiments.

Now, we describe the image update step. Non-linearity and non-differentiability make the problem (3.2.1) difficult to be solved. Thus, we use the alternating direction method of multipliers (ADMM) [62], which actually solves the following linearly constrained reformulation of (3.2.1):

$$\begin{aligned} &(1-g)\nu_1(\nabla u^k)\|\mathbf{v}\|_2 + g\nu_2(\nabla^2 u^k)\|\mathbf{w}\|_2 + \frac{\mu}{2}\|u-f\|_2^2, \\ &\text{s.t.}\ \ \mathbf{v}=\nabla u,\ \mathbf{w}=\nabla^2 u, \end{aligned} \tag{3.2.2}$$

where $\mathbf{v}\in Q$ and $\mathbf{w}\in Z$. The framework of ADMM for solving (3.2.1) is shown below.

First, we define the following augmented Lagrangian function:

$$\begin{aligned} \mathcal{L}(\mathbf{v},\mathbf{w},u;\lambda,\tau) &= (1-g)\nu_1(\nabla u^k)\|\mathbf{v}\|_2 - \lambda^\top(\mathbf{v}-\nabla u) + \frac{\beta}{2}\|\mathbf{v}-\nabla u\|_2^2 \\ &+ g\nu_2(\nabla^2 u^k)\|\mathbf{w}\|_2 - trace(\tau^\top(\mathbf{w}-\nabla^2 u)) + \frac{\gamma}{2}\|\mathbf{w}-\nabla^2 u\|_2^2 + \frac{\mu}{2}\|u-f\|_2^2 \end{aligned} \tag{3.2.3}$$

where $\lambda\in Q$ and $\tau\in Z$ are the Lagrange multipliers, and β and γ are positive constants. Then, we alternatively solve (3.2.3) with respect to $\mathbf{v}$, $\mathbf{w}$ and u and then update the multipliers:

$$\begin{cases} \mathbf{v}^{k+1} \leftarrow \arg\min_{\mathbf{v}} \mathcal{L}(\mathbf{v},\mathbf{w},u^k;\lambda^k,\tau^k) \\ \mathbf{w}^{k+1} \leftarrow \arg\min_{\mathbf{w}} \mathcal{L}(\mathbf{v},\mathbf{w},u^k;\lambda^k,\tau^k) \\ u^{k+1} \leftarrow \arg\min_{u} \mathcal{L}(\mathbf{v}^{k+1},\mathbf{w}^{k+1},u;\lambda^k,\tau^k) \\ \lambda^{k+1} \leftarrow \lambda^k - \beta(\mathbf{v}^{k+1}-\nabla u^{k+1}) \\ \tau^{k+1} \leftarrow \tau^k - \gamma(\mathbf{w}^{k+1}-\nabla u^{k+1}) \end{cases}$$

The minimization of $\mathcal{L}$ with respect to $\mathbf{v}$ is expressed as the following simple form:

$$\min_{\mathbf{v}}\ (1-g)\nu_1(\nabla u)\|\mathbf{v}\|_2 + \frac{\beta}{2}\|\mathbf{v}-(\nabla^k u+\frac{\lambda^k}{\beta})\|_2^2 \tag{3.2.4}$$

The solution of (3.2.4) is given by a generalized shrinkage formula defined in

[71]:

$$\begin{aligned}\mathbf{v}_i^{k+1} &= shrink\left(\nabla u_i^k + \frac{\lambda_i^k}{\beta}, \frac{(1-g)\nu_1(\nabla u_i^k)}{\beta}\right) \\ &= \max\left\{\|\nabla u_i^k + \frac{\lambda_i^k}{\beta}\|_2 - \frac{(1-g)\nu_1(\nabla u_i^k)}{\beta}, 0\right\} \frac{\nabla u_i^k + \frac{\lambda_i^k}{\beta}}{\|\nabla u_i^k + \frac{\lambda_i^k}{\beta}\|_2} \quad (3.2.5) \\ \text{for} \quad & i = 1, \cdots, N^2\end{aligned}$$

Similarly, we can obtain the minimizer of $\mathcal{L}$ with respect to $\mathbf{w}$ as follows:

$$\begin{aligned}\mathbf{w}_i^{k+1} &= shrink\left(\nabla^2 u_i^k + \frac{\tau_i^k}{\gamma}, \frac{g\nu_2(\nabla^2 u_i^k)}{\gamma}\right) \\ &= \max\left\{\|\nabla^2 u_i^k + \frac{\tau_i^k}{\gamma}\|_2 - \frac{g\nu_2(\nabla^2 u_i^k)}{\gamma}, 0\right\} \frac{\nabla^2 u_i^k + \frac{\tau_i^k}{\gamma}}{\|\nabla^2 u_i^k + \frac{\tau_i^k}{\gamma}\|_2} \quad (3.2.6) \\ \text{for} \quad & i = 1, \cdots, N^2\end{aligned}$$

The minimization of $\mathcal{L}$ with respect to u gives the following least squares problem:

$$\min_u \frac{\beta}{2}\|(\mathbf{v}^{k+1} - \frac{\lambda^k}{\beta}) - \nabla u\|_2^2 + \frac{\gamma}{2}\|(\mathbf{w}^{k+1} - \frac{\tau^k}{\gamma}) - \nabla^2 u\|_2^2 + \frac{\mu}{2}\|u - f\|_2^2 \quad (3.2.7)$$

and the corresponding normal equation is

$$(\beta\nabla^\top\nabla + \gamma(\nabla^2)^\top\nabla^2 + \mu)u = \beta\nabla^\top(\mathbf{v}^{k+1} - \frac{\lambda^k}{\beta}) + \gamma(\nabla^2)^\top(\mathbf{w}^{k+1} - \frac{\tau^k}{\gamma}) + \mu f \quad (3.2.8)$$

Under the periodic boundary condition of u, the above linear system can be efficiently solved by using fast fourier transform (FFT). Because we assume the reflexive boundary condition of u, we can adopt discrete cosine transform (DCT) [14, 49, 50] instead of FFT.

We can attach a steplength $\delta \in (0, (\sqrt{5}+1)/2)$ to update the multipliers λ and τ:

$$\lambda^{k+1} = \lambda^k - \delta\beta(\mathbf{v}^{k+1} - \nabla u^{k+1}) \quad (3.2.9)$$

$$\tau^{k+1} = \tau^k - \delta\gamma(\mathbf{w}^{k+1} - \nabla^2 u^{k+1}) \quad (3.2.10)$$

as done in [62]. The algorithmic framework for solving the non-convex hybrid TV model is described in Algorithm 3.

Algorithm 3: Non-convex hybrid TV model

Input: Given noisy image f, parameter: μ, β, γ, η and stopping criterion: ϵ, M_1, M_2

Initialization: $u^0 = f, \lambda^0 = 0, \tau^0 = 0$

For $n = 1 : M_1$ do

update weight: $\nu_1^n(\nabla u^{n-1}) = \|\nabla u^{n-1} + \eta\|_2^{\alpha_1 - 1}$,
$\nu_2^n(\nabla^2 u^{n-1}) = \|\nabla^2 u^{n-1} + \eta\|_2^{\alpha_2 - 1}$

For $k = 1 : M_2$

update v: $\mathbf{v}^k = shrink(\nabla u^{k-1} + \frac{\lambda^{k-1}}{\beta}, \frac{(1-g)\nu_1(\nabla u^{k-1})}{\beta})$

update w: $\mathbf{w}^k = shrink(\nabla^2 u^{k-1} + \frac{\tau^{k-1}}{\gamma}, \frac{g\nu_2(\nabla^2 u^{k-1})}{\gamma})$

update u:

$(\beta\nabla^\top\nabla + \gamma(\nabla^2)^\top\nabla^2 + \mu)u^k =$
$\beta\nabla^\top(\mathbf{v}^k - \frac{\lambda^{k-1}}{\beta}) + \gamma(\nabla^2)^\top(\mathbf{w}^k - \frac{\tau^{k-1}}{\gamma}) + \mu f$

update λ: $\lambda^k = \lambda^{k-1} - \delta\beta(\mathbf{v}^k - \nabla u^k)$

update τ: $\tau^k = \tau^{k-1} - \delta\gamma(\mathbf{w}^k - \nabla^2 u^k)$

end For

if $||u^n - u^{n-1}||/||u^n|| < \epsilon$

return

end if

end For

3.3 Numerical experiments

We performed experiments on several images including the well-known Barbara, Cameraman and Lena, as seen in Figure 3.2, to show the performance of our proposed model. All numerical experiments were performed on 64-bit Window 7 on a desktop with an Intel CPU at 3.50 GHz and 16 GB memory. The additive noise was Gaussian with various standard deviations σ. We implemented our IRHTV by using MATLAB R2011b (version

7.13.0.564). We use SNR as the image quality measure that is defined as

$$SNR(\tilde{u}, u) = 10 * \log_{10}(\frac{\|u - \bar{u}\|^2}{\|u - \tilde{u}\|^2})$$

where u is the original image, $\bar{u}$ is the mean intensity value of u, and $\tilde{u}$ is the restored image. We also adopt the SSIM to measure the similarity between two images [70], which is defined as

$$SSIM(\tilde{u}, u) = \frac{(2\mu_{\tilde{u}}\mu_u + c_1)(2\sigma_{\tilde{u}u} + c_2)}{(\mu_{\tilde{u}}^2 + \mu_u^2 + c_1)(\sigma_{\tilde{u}}^2 + \sigma_u^2 + c_2)}$$

where μ_u is the average of u, σ_u^2 is the variance of u, $\sigma_{\tilde{u}u}$ is the covariance of $\tilde{u}$ and u and c_1, c_2 are two constants to avoid instability. We terminate every algorithm by the following stopping criterion:

$$\frac{\|u^k - u^{k-1}\|}{\|u^k\|} \leq \epsilon \text{ or iteration number} \leq M, \tag{3.3.1}$$

where ϵ is a given positive tolerance and M is the maximum number of iterations. We assume that the image intensity range is $[0, 1]$.

3.3.1 Parameter values

The speed of convergence is related to β for the non-convex TV model and γ for the non-convex HOTV model. Figure 3.3 shows the relation between the speed of convergence and γ for the non-convex HOTV model. As β and γ increase, SNR tends to increase slightly but the algorithms take additional time to terminate. There is a trade-off between computational costs and the SNR value. To balance the SNR value and the speed of convergence, β and γ values of around 10 are suitable; see Figure 3.3 and Figure 3.4, and hence we choose $\beta = 10$ and $\gamma = 10$. We set the steplength $\delta = 1.618$ in all experiments [62]. μ is determined by experiments and is influenced by the noise level and values of α_1 and α_2. This value tends to increase with decreasing noise level and decreasing α_1 and α_2 . We use the stopping criteria summarized in Table 3.1 for all experiments unless stated otherwise. To incur less computational cost, we use a fixed maximum number of iterations for the inner loop of the IRHTV algorithm.

(a) Barbara (b) Cameraman (c) Clock (d) House (e) Lena

(f) Parrot (g) Boats (h) Child (i) Man (j) Peppers

Figure 3.2: Test images for experiments. (a)-(f): Size 256×256, (g)-(j): Size 512×512

Table 3.1: Stopping Criteria

Regularizer	Non-convex model ($\alpha < 1$)		Convex model ($\alpha = 1$)
	Outer loop	Inner loop	.
$\|\nabla u\|_2^\alpha$	$\epsilon = 1.e-2, M_1 = 100$	$M_2 = 5$	$\epsilon = 5.e-4, M = 100$
$\|\nabla^2 u\|_2^\alpha$	$\epsilon = 5.e-3, M_1 = 100$	$M_2 = 20$	$\epsilon = 1.e-4, M = 100$
$(1-g)\|\nabla u\|_2^{\alpha_1} + g\|\nabla^2 u\|_2^{\alpha_2}$	$\epsilon = 5.e-3, M_1 = 100$	$M_2 = 20$	$\epsilon = 1.e-4, M = 100$

In following subsection 3.3.2, we compare the proposed model with the ROF, LLT and hybrid TV model. We apply the ADMM algorithm for solving the ROF, LLT and hybrid TV model. In all experiments for convex models, we use the same parameter values, $\beta = 10$, $\gamma = 10$ and $\delta = 1.618$ as for non-convex models. We also use the stopping criteria summarized in Table 3.1 for convex models.

3.3.2 Comparison between the non-convex TV model and the non-convex HOTV model

In this subsection, we compare the non-convex HOTV model (3.1.1) with the following non-convex TV model, in which the TV regularizer of the ROF model is replaced by $\|\nabla u\|_2^\alpha$.

$$\min_u \|\nabla u\|_2^\alpha + \frac{\mu}{2}\|u-f\|_2^2 \qquad (\alpha < 1) \tag{3.3.2}$$

We minimize energy (3.3.2) by using IRHTV. From Figure 3.5d and Figure 3.5e, as α decreases, TV becomes sparser. That is, noisy nonzero gradients disappear, and restored images become more cartoon-like. The following L_0 gradient minimization is an extreme case.

$$\min_u \; C(u) + \frac{\mu}{2}\|u-f\|_2^2 \;\text{ where }\; C(u) = \sharp\{p \,||\partial_x u|_p + |\partial_y u|_p \neq 0\} \tag{3.3.3}$$

This model enhances edges by confining the number of nonzero gradients using the above anisotropic regularizer. Xu et al. [74] dealt with this non-convex and non-smooth problem by using the penalty approximation with two closed form solutions. Because the first closed form solution is related to thresholding, we can see that its result is sensitive to severe noise and tends to sharpen the edges and noises more than required; see Figure 3.5f.

L_0 gradient minimization was implemented by using an online source code from http://www.cse.cuhk.edu.hk/∼leojia/projects/L0smoothing.

The ROF model preserves sharp edges but becomes blocky to cause distortions in homogeneous regions because of severe noise; see Figure 3.5c. On the other hand, the non-convex TV model with $\alpha = 0.8$ makes the TV sparser and therefore, the artifacts in homogeneous regions disappear, edges are sharper, and the best SNR value is obtained; see Figure 3.5d. It is noteworthy that the non-convex TV model is superior to the ROF model for denoising an image dominated by piecewise constant regions and sharp edges. However the non-convex TV model may flatten even smooth regions. Tables 3.2 and 3.3 show that the ROF model operates more efficiently than the non-convex TV model for overall smooth images, e.g., Lena, Child, and Peppers. This is because as the image gradient becomes sparser, smooth transition regions

Table 3.2: SNR(dB), SSIM, Time(in seconds) and the numbers of iterations of TV, non-convex(NC) TV, HOTV, non-convex HOTV, hybrid TV and non-convex hybrid TV with a high noise level ($\sigma = 2.e-1$).

	$\|\nabla u\|^{\alpha_1}$		$\|\nabla^2 u\|^{\alpha_2}$		$\frac{1}{2}\|\nabla u\|^{\alpha_1} + \frac{1}{2}\|\nabla^2 u\|^{\alpha_2}$	
Model	NC TV	ROF	NC HOTV	LLT	NC Hybrid TV	Hybrid TV
α_1	0.9	1	·	·	0.9	1
α_2	·	·	0.7	1	0.7	1
μ	8	6	25	9	18	8
Image	SNR/SSIM/Time/Itr.	SNR/SSIM/Time/Itr.	SNR/SSIM/Time/Itr.	SNR/SSIM/Time/Itr.	SNR/SSIM/Time/Itr.	SNR/SSIM/Time/Itr.
Barbara	8.96/0.5846/0.38/5	9.07/0.5960/0.41/24	9.37/0.6243/2.85/8	9.06/0.6061/0.73/37	9.55/0.6359/3.43/7	9.27/0.6173/1.50/58
Cameraman	11.46/0.6990/0.40/5	11.29/0.6915/0.37/24	11.77/0.7144/2.50/7	10.79/0.6563/0.76/39	12.05/0.7256/3.42/7	11.26/0.6946/1.58/60
Clock	11.72/0.8234/0.30/4	11.69/0.8263/0.32/21	12.33/0.8502/1.77/5	11.76/0.8139/0.69/35	12.52/0.8592/2.46/5	12.01/0.8418/1.45/55
House	11.94/0.7543/0.36/5	11.92/0.7493/0.36/23	12.40/0.7659/2.48/7	11.76/0.7150/0.70/36	12.79/0.7813/3.39/7	12.40/0.7614/1.43/55
Lena	10.61/0.7191/0.39/5	10.72/0.7232/0.37/24	11.23/0.7567/2.48/7	10.86/0.7212/0.73/37	11.45/0.7660/3.39/7	11.21/0.7467/1.47/57
Parrot	11.44/0.6957/0.37/5	11.33/0.6964/0.37/24	12.17/0.7299/2.49/7	11.39/0.6998/0.77/39	12.29/0.7322/3.42/7	11.65/0.7160/1.52/58
Boats	10.23/0.7546/3.57/5	10.29/0.7559/3.39/24	10.75/0.7730/24.45/7	10.36/0.7437/6.81/37	10.93/0.7820/32.11/7	10.66/0.7675/13.67/57
Child	14.64/0.7860/2.74/4	14.81/0.7912/3.22/23	15.32/0.8069/21.24/6	15.22/0.7817/7.08/37	15.32/0.8135/27.76/6	15.32/0.8057/12.97/54
Man	9.63/0.6325/3.41/5	9.73/0.6431/3.64/26	10.22/0.6664/27.73/8	10.19/0.6798/7.88/43	10.21/0.6608/36.61/8	10.15/0.6687/14.37/60
Peppers	12.85/0.8364/3.41/5	12.90/0.8328/3.36/24	13.75/0.8528/24.56/7	13.08/0.7922/7.01/38	13.74/0.8612/32.20/7	13.32/0.8348/13.66/57
Average	11.35/0.7285/1.53/ 5	11.37/0.7306/1.58/ 24	11.93/0.7540/11.26/ 7	11.45/0.7210/3.32/ 38	12.08/0.7618/14.82/ 7	11.72/0.7455/6.36/ 57

convert into piecewise constant regions thereby causing staircase artifacts; see Figure 3.1b and 3.1c.

Meanwhile, we can confirm that the non-convex HOTV model with $\alpha =$ 0.7 produces the best SNR value and the highest visual quality for all tested images, as given by Tables 3.2 and 3.3. Figure 3.6d–3.6f show the effect of the non-convex HOTV regularizer. Since the non-convex HOTV makes the support of HOTV sparse, the image intensity changes more smoothly for a smaller α. We can see that staircase artifacts, which are the side-effects of the TV regularizer, disappear when the non-convex HOTV regularizer is used. However, it may not maintain edges correctly because of the HOTV characteristic that promotes piecewise linear solutions. In summary, the non-convex TV model obtains better results for a specific range of images. In contrast, the non-convex HOTV model obtains better results for a wider range of images in terms of the recovery of smooth regions.

3.3.3 Comparison with other non-convex higher order regularizers.

Before demonstrating the performance of the non-convex hybrid TV model, we compare non-convex HOTV with different non-convex regularizers for

Table 3.3: SNR(dB), SSIM, Time(in seconds) and the numbers of iterations of TV, non-convex(NC) TV, HOTV, non-convex HOTV, hybrid TV and non-convex hybrid TV with a low noise level($\sigma = 7.e-2$)

	$\|\nabla u\|^{\alpha_1}$		$\|\nabla^2 u\|^{\alpha_2}$		$\frac{1}{2}\|\nabla u\|^{\alpha_1} + \frac{1}{2}\|\nabla^2 u\|^{\alpha_2}$	
Model	NC TV	ROF	NC HOTV	LLT	NC Hybrid TV	Hybrid TV
α_1	0.9	1	·	·	0.9	1
α_2	·	·	0.7	1	0.7	1
μ	27	20	93	38	59	29
Image	SNR/SSIM/Time/Itr.	SNR/SSIM/Time/Itr.	SNR/SSIM/Time/Itr.	SNR/SSIM/Time/Itr.	SNR/SSIM/Time/Itr.	SNR/SSIM/Time/Itr.
Barbara	13.47/0.8103/0.24/3	13.42/0.8103/0.16/10	14.62/0.8551/0.73/4	13.94/0.8290/0.30/15	14.50/0.8509/1.02/4	13.95/0.8318/0.57/21
Cameraman	17.27/0.8487/0.23/3	17.10/0.8432/0.16/10	17.64/0.8581/0.91/5	16.76/0.8303/0.32/16	17.78/0.8640/1.02/4	17.20/0.8496/0.56/21
Clock	18.16/0.9044/0.16/2	18.01/0.9000/0.14/9	18.68/0.9141/0.75/4	17.77/0.8779/0.27/13	19.00/0.9282/1.01/4	18.29/0.9044/0.49/18
House	16.99/0.8400/0.22/3	16.95/0.8360/0.16/10	17.38/0.8465/0.92/5	16.76/0.8194/0.28/14	17.73/0.8551/1.02/4	17.33/0.8414/0.55/20
Lena	15.56/0.8579/0.23/3	15.60/0.8566/0.16/10	16.39/0.8840/0.92/5	15.89/0.8615/0.28/14	16.54/0.8874/1.03/4	16.18/0.8725/0.54/20
Parrot	17.51/0.8491/0.22/3	17.42/0.8476/0.16/10	18.06/0.8654/0.92/5	17.37/0.8474/0.30/15	18.18/0.8685/1.05/4	17.72/0.8590/0.57/21
Boats	14.90/0.9093/2.05/3	14.94/0.9083/1.42/10	15.61/0.9175/8.88/5	15.26/0.9037/2.60/14	15.69/0.9208/9.36/4	15.45/0.9135/4.86/20
Child	20.39/0.9156/2.05/3	20.54/0.9144/1.28/9	21.33/0.9204/7.07/4	21.15/0.9060/2.42/13	21.43/0.9272/9.41/4	21.31/0.9189/4.64/19
Man	15.29/0.8670/2.09/3	15.38/0.8707/1.58/11	16.12/0.8861/8.82/5	16.03/0.8879/2.79/15	16.05/0.8790/11.69/5	16.01/0.8846/5.17/21
Peppers	17.86/0.9303/2.12/3	17.78/0.9266/1.43/10	18.69/0.9314/8.81/5	17.88/0.9056/2.78/15	18.65/0.9393/9.41/4	17.95/0.9238/4.89/20
Average	16.74/0.8733/0.96/3	16.72/0.8714/0.66/10	17.45/0.8879/3.87/5	16.88/0.8669/1.24/14	17.56/0.8921/4.60/4	17.14/0.8799/2.28/20

higher order derivatives using different algorithms respectively. Although non-convex variational models with first order derivative have been studied previously as reviewed in the subsection 2.1.4, to the best of our knowledge, no research has been conducted on a non-convex variational model with higher order derivatives thus far.

This comparison contributes greatly to demonstrate the effect of introducing the non-convexity of higher order derivatives and illustrate the efficiency of IRHTV for the non-convex regularizer.

We consider the following non-convex higher order model.

$$\min_u \int \phi(|\nabla^2 u|) + \frac{\mu}{2}\|u - f\|_2^2 \tag{3.3.4}$$

To solve the above problem (3.3.4), we use three algorithms for different non-convex potentials mentioned in the subsection 2.1.4 and the section 3.2. The half-quadratic algorithm and non-smooth GNC algorithm applied to the first order derivatives can be extended to the higher order derivatives. The list of non-convex potential functions and corresponding algorithms is below.

1. The half-quadratic(HQ) algorithm : $\phi(|\nabla^2 u|) = \frac{\alpha|\nabla^2 u|^2}{1+\alpha|\nabla^2 u|^2}$
2. Non-smooth GNC algorithm : $\phi(|\nabla^2 u|) = \frac{\alpha|\nabla^2 u|}{1+\alpha|\nabla^2 u|}$

3. Our proposed model and algorithm(IRHTV) : $\phi(|\nabla^2 u|) = |\nabla^2 u|^\alpha$

In Figure 3.7, $\phi(t) = \frac{\alpha t^2}{1+\alpha t^2}$ solving by HQ algorithm poorly works, against expectation. But the non-convex regularizers for higher order derivatives, $\phi(t) = t^\alpha$ and $\phi(t) = \frac{\alpha t}{1+\alpha t}$ result in the better denoised image and lead to better SNR value than the convex HOTV regularizer $\phi(t) = t$, the LLT model. The superiority of non-convex HOTV and IRHTV deserves special emphasis.

3.3.4 Comparison between two non-convex hybrid TV models

In this subsection, we present the performance of two non-convex hybrid TV models. Numerical results demonstrate that the convex combination model (3.1.3) performs slightly better than the model using an edge detection function (3.1.4). The convex combination of the non-convex TV and non-convex HOTV regularizers with the same weight achieves the best performance as observed by our experiments.

In Table 3.2, we list the SNR values for the ROF, LLT, hybrid TV, non-convex TV, non-convex HOTV and non-convex hybrid TV models for 10 images, and the average SNR value of all images to show the efficiency of the proposed models. For the non-convex model, Itr. indicates the outer iteration number. As expected, the visual quality and SNR value are improved significantly when the non-convex HOTV regularizer is used. Moreover, the combination of the non-convex TV regularizer with the non-convex HOTV regularizer compensates for the defect in the non-convex HOTV regularizer and therefore, the best SNR value is obtained. In Figure 3.1e and Figure 3.1f as an example, we can confirm that the non-convex hybrid TV regularizer preserves the step edges better than the non-convex HOTV regularizer. Therefore, the model that combines the non-convex TV regularizer with the non-convex HOTV regularizer performs better than the model with only the non-convex HOTV regularizer or only the non-convex TV regularizer.

Table 3.3 summarizes results with different noise level. For a low noise level, we modify the stopping criterion slightly to consider the computational cost and SNR value. We set $\epsilon = 1.e-3$ in (3.3.1) for the ROF model and

$\epsilon = 5.e-4$ in (3.3.1) for the HOTV and hybrid TV models. We fixed the maximum number of iterations of the inner loop, M_2, as 10 in the IRHTV algorithm for the non-convex HOTV and non-convex hybrid TV models. A non-convex HOTV is well-suited for image denoising, and in particular, a combination of two non-convex regularizers leads to more favorable results.

Figure 3.8 and Figure 3.9 show denoising results corresponding to Table 3.2, which demonstrate the efficiency of the non-convex hybrid TV model. Furthermore, Figure 3.10 and 3.11 corresponding to Table 3.3 show the superiority of our model to other models. The Lena image has characteristics similar to a 1D signal in Figure 3.1 which is composed of piecewise smooth regions and piecewise constant regions. When we apply the non-convex hybrid TV model to the Lena image in Figure 3.10, the SNR value and visual quality are improved significantly as in the case of the 1D signal. Moreover, Our model is well-suited for an image that consists mainly piecewise constant regions, e.g., Cameraman image in Figure 3.11.

3.3.5 Comparison with Krishnan et al. [39]

Until now, we focus on the isotropic case of the non-convex TV and non-convex higher order TV regularizer. But now, we consider an anisotropic case for the non-convex TV and non-convex higher order TV regularizer. In [39], Krishnan et al. suggested the analytic solution of sub-problem for non-convex anisotropic TV prior, by finding the roots of a cubic polynomial for $\alpha = \frac{1}{2}$ and quartic polynomial for $\alpha = \frac{2}{3}$. We compare our results with the results of [39] to present the stability and accuracy of IRHTV scheme. We consider the case that constant g is $\frac{1}{2}$, α_1 is 1 and α_2 is $\frac{2}{3}$. To implement the non-convex hybrid TV model (3.1.3) without relaxation using Krishnan et al.'s idea, we use their codes in our framework, downloading it at
http://cs.nyu.edu/∼dilip/research/fast-deconvolution. We summarize our algorithm in Algorithm 4.

In Figure 3.12, we can affirm that IRHTV scheme has about the same SNR value as well as similar visual quality to results gotten from analytic solutions without the convex relaxation. The benefits of IRHTV scheme are that the practical implementation of non-convex problem is possible for any

Algorithm 4 : ADMM without relaxation for non-convex hybrid TV model

Input : Given noisy image f , parameter : μ, β, γ and stopping criterion : ϵ, M

Initialization :$u^0 = f, \lambda^0 = 0, \tau^0 = 0$

For n = 1: M do

solve v : $\exists$ analytic solution for $\alpha_1 = 1, \frac{1}{2}, \frac{2}{3}$.

solve w : $\exists$ analytic solution for $\alpha_2 = 1, \frac{1}{2}, \frac{2}{3}$.

update u :

$$(\beta\nabla^\top\nabla + \gamma(\nabla^2)^\top\nabla^2 + \mu)u = \beta\nabla^\top(\mathbf{v^n} - \tfrac{\lambda^{n-1}}{\beta}) + \gamma(\nabla^2)^\top(\mathbf{w^n} - \tfrac{\tau^{n-1}}{\gamma}) + \mu f$$

update λ : $\lambda^n = \lambda^{n-1} - \delta\beta(\mathbf{v^n} - \nabla u^n)$

update τ : $\tau^n = \tau^{n-1} - \delta\gamma(\mathbf{w^n} - \nabla^2 u^n)$

if $||u^n - u^{n-1}||/||u^n|| < \epsilon$

return

end if

end For

α value and it can achieve higher accuracy. And, we can observe that non-convex hybrid TV model with $\alpha_1 = 0.9, \alpha_2 = 0.7$ (Table 3.2) yields even higher SNR value (SNR=11.45) for the same degraded image (Figure 3.12b) than anisotropic case (Figure 3.12c and 3.12d).

3.3.6 Comparison with state-of-the-art

In this subsection, we are interested in comparing the non-convex hybrid TV model with three state-of-the-art image denoising models. Extensive numerical results demonstrate that our model performs favorably in comparison to these state-of-the-art image denoising models.

Comparison with Nonlocal TV

First, we compare the proposed model with Nonlocal(NL) TV model as state-of-the-art [78]. To test NLTV model, we use the MATLAB and MEX function implementation and the default parameter from
http://www.cs.cityu.edu.hk/∼xbresson/ucla/code.html.

Comparing with Figure 3.13e with Figure 3.13f, we can observe that NLTV works better than non-convex hybrid TV for textured images. But Figure 3.13 shows that the proposed model is superior to NLTV for a wide range of images. So, our model is considered as competitive model with NLTV

model.

Comparison with TGV2

We compare the denoised performance of the proposed model with the TGV model, which was mentioned in the subsection 2.1.2. For a fair comparison, we adopt the second order TGV. We use the TGV^2 denoising model (2.1.9), which is solved by a first-order primal-dual algorithm [18]. It's known that higher order TGV results in better denoising images but the computational burden may increase.

As shown in Figure 3.14, we observed that TGV^2 achieves better SNR value than ROF and LLT, but lower value than the proposed model. But, in visual quality, the proposed model and TGV^2 produce similar results. To compare the computational cost, we measure the CPU time under the same stopping criterion. For a smaller size image, Figure 3.14d, the computational cost of our model and TGV^2 model is not significantly different, but for the large size image, TGV^2 outperforms our model due to its convexity in Figure 3.14h.

Comparison with BM3D

Lastly, we compare the proposed model with block-matching and 3D filtering (BM3D) [31], which is a state of the art denoising method.

Based on the fact that an image has a locally sparse representation in transform-domain, BM3D enhances the sparsity by grouping similar 2D image blocks into 3D groups. To test BM3D algorithm, we use the MATLAB code along MEX function implementation from http://www.cs.tut.fi/∼foi/GCF-BM3D/. Numerical results show that the non-convex hybrid TV model is not competitive with BM3D. Nevertheless, a fair and precise comparison with this state of the art denoising method needs to be done in order to evaluate the capacity of the proposed models.

As shown in Figure 3.15, we can observe that BM3D works better than the non-convex hybrid TV. But, the proposed model is still novel considering that it has significant improvement on the other TV-type models.

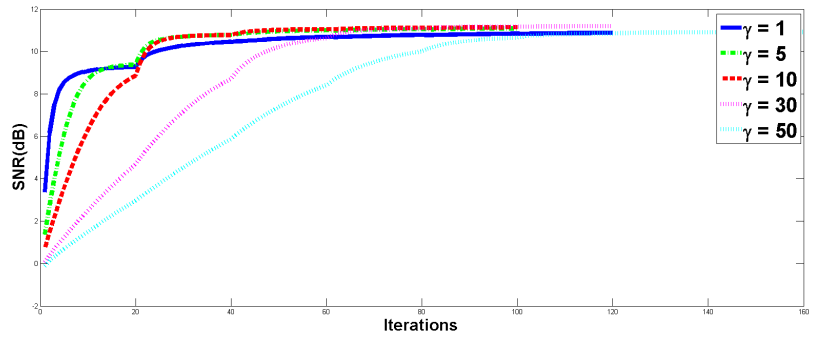

(a)

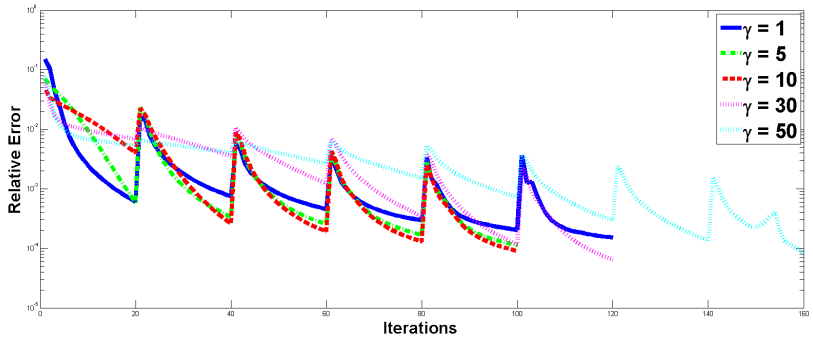

(b)

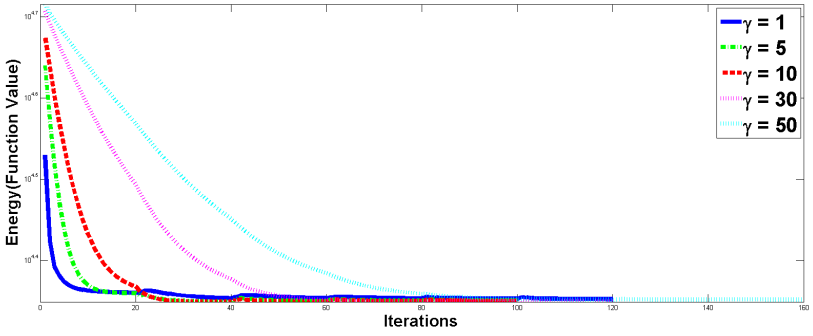

(c)

Figure 3.3: The performance of the non-convex HOTV ($\alpha = 0.8$) corresponding to a set of γ values $= [1, 5, 10, 30, 50]$. The speed of convergence is related to γ for the non-convex HOTV model. (a) SNR value (b) Relative error (c) Function value

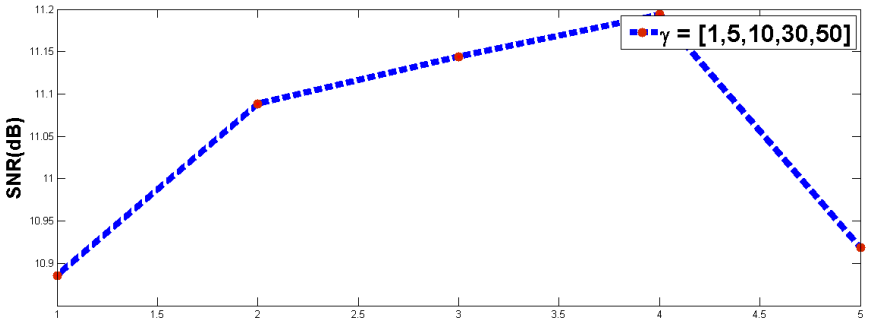

(a)

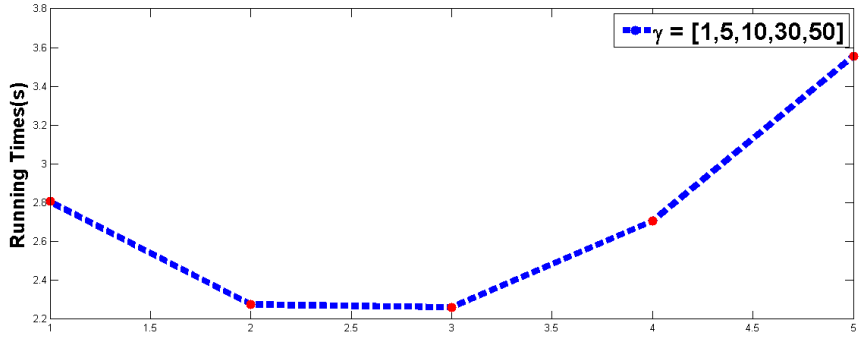

(b)

Figure 3.4: (a)SNR and (b)Running Times : results of ADMM for high order TV model($\alpha = 0.8$) corresponding to a set of γ values = [1,5,10,30,50]. Too small or too big γ values make the speed of convergence slow. Suitable γ value's range may be from 1 to 50 and we set $\gamma = 10$ in all tests.

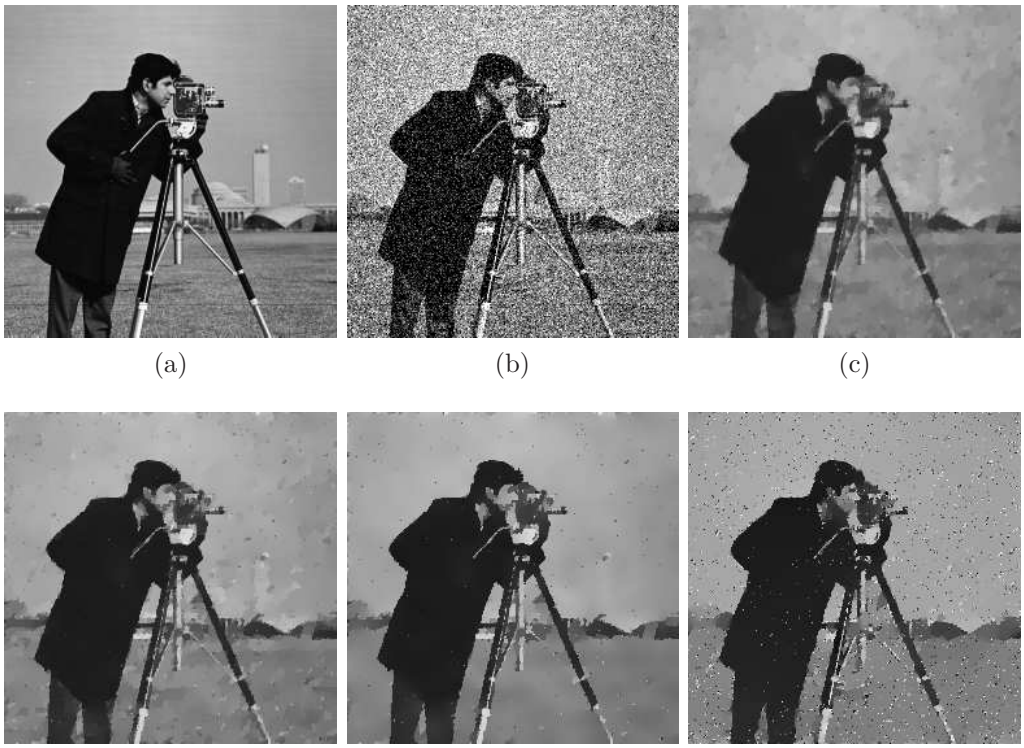

(a) (b) (c)

(d) (e) (f)

Figure 3.5: Comparison of non-convex TV with ROF, and L_0 gradient minimization: For the image mainly dominated by piecewise constant regions, the non-convexity of TV ($\alpha = 0.8$) yields better results than the original convex TV. We use ADMM to solve the ROF model. (a) Original image (b) Noisy image, (SNR(dB), SSIM)=(2.52, 0.1897) (c) ROF, (SNR(dB), SSIM)= (11.29, 0.6915) (d) Non-convex TV with α =0.8, (SNR(dB), SSIM)=(11.54, 0.6869) (e) Non-convex TV with α =0.4, (SNR(dB), SSIM)=(11.15, 0.6783) (f) L_0 gradient minimization, (SNR(dB), SSIM)=(8.24, 0.4652)

(a) (b) (c)

(d) (e) (f)

Figure 3.6: Comparison between LLT and the non-convex HOTV. The non-convexity of HOTV ($\alpha = 0.7$) improves the SNR value and facilitates smooth transitions in intensity. We adopt ADMM to solve LLT model. (a) Original image (b) Noisy image, (SNR(dB), SSIM) = (-0.15, 0.1704) (c) LLT, (SNR(dB), SSIM) = (10.86, 0.7212) (d) Non-convex HOTV with α =0.9, (SNR(dB), SSIM) = (11.01, 0.7345) (e) Non-convex HOTV with α =0.7, (SNR(dB), SSIM) = (11.23, 0.7567) (f) Non-convex HOTV with α =0.5, (SNR(dB), SSIM) = (10.56, 0.7276)

(a) Original (b) Noisy (c) LLT

(d) $\phi(t) = |t|^{0.7}$ (e) $\phi(t) = \frac{200|t|^2}{1+200|t|^2}$ (f) $\phi(t) = \frac{1.5|t|}{1+1.5|t|}$

Figure 3.7: Comparison of the non-convex regularizers for higher order derivatives with LLT. (a) Original image (b) Noisy, SNR = -0.15 (c) SNR = 10.86 (d) SNR = 11.23 (e) SNR = 10.52 (f) SNR = 11.00. We adopt ADMM for LLT, IRHTV for $\phi(t) = |t|^{\alpha}$, HQ for $\phi(t) = \frac{\alpha|t|^2}{1+\alpha|t|^2}$, and GNC algorithm for $\phi(t) = \frac{\alpha|t|}{1+\alpha|t|}$ respectively.

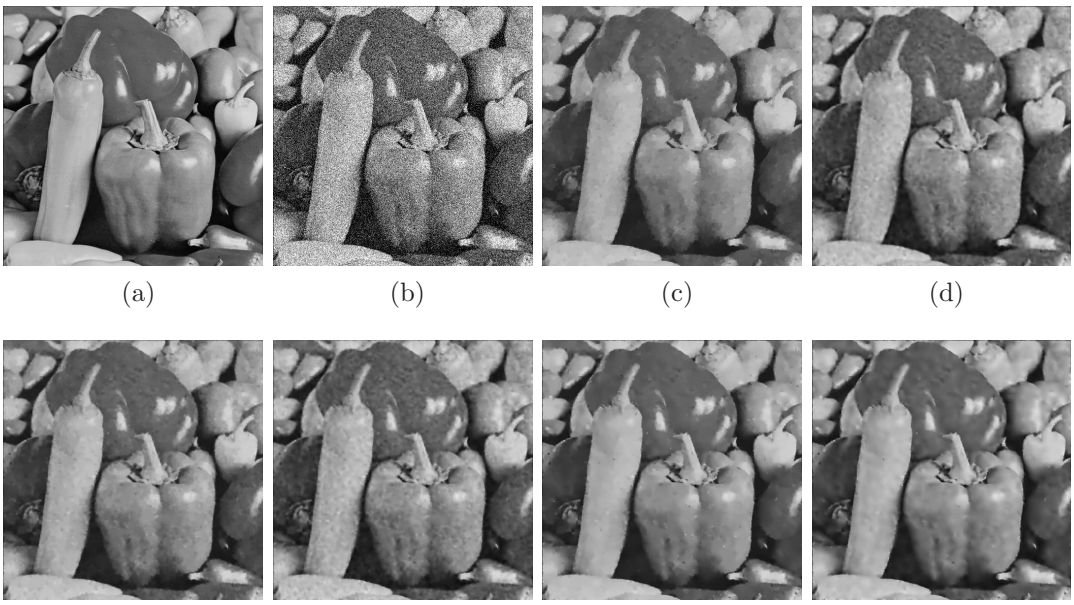

(a) (b) (c) (d)

(e) (f) (g) (h)

Figure 3.8: Comparison of the non-convex hybrid TV with ROF, LLT, and hybrid TV with a high noise level($\sigma = 2.e - 1$). Because the Peppers image contains smooth regions and edges, the non-convex hybrid TV is well-suited to this image. (a) Original image (b) Noisy image, (SNR(dB), SSIM) = (1.05, 0.3558) (c) ROF, (SNR(dB), SSIM) = (12.90, 0.8328) (d) LLT, (SNR(dB), SSIM) = (13.08, 0.7922) (e) Hybrid TV with $\alpha_1 = 1, \alpha_2 = 1, g = \frac{1}{2}$, (SNR(dB), SSIM) = (13.32, 0.8348) (f) Hybrid TV with $\alpha_1 = 1, \alpha_2 = 1$, $g =$ edge detection function, (SNR(dB), SSIM) = (13.03, 0.7958) (g) Non-convex hybrid TV with $\alpha_1 = 0.9, \alpha_2 = 0.7, g = \frac{1}{2}$, (SNR(dB), SSIM) = (13.74, 0.8612) (h) Non-convex hybrid TV with $\alpha_1 = 0.9, \alpha_2 = 0.7$, $g =$ edge detection function, (SNR(dB), SSIM) = (13.74, 0.8574)

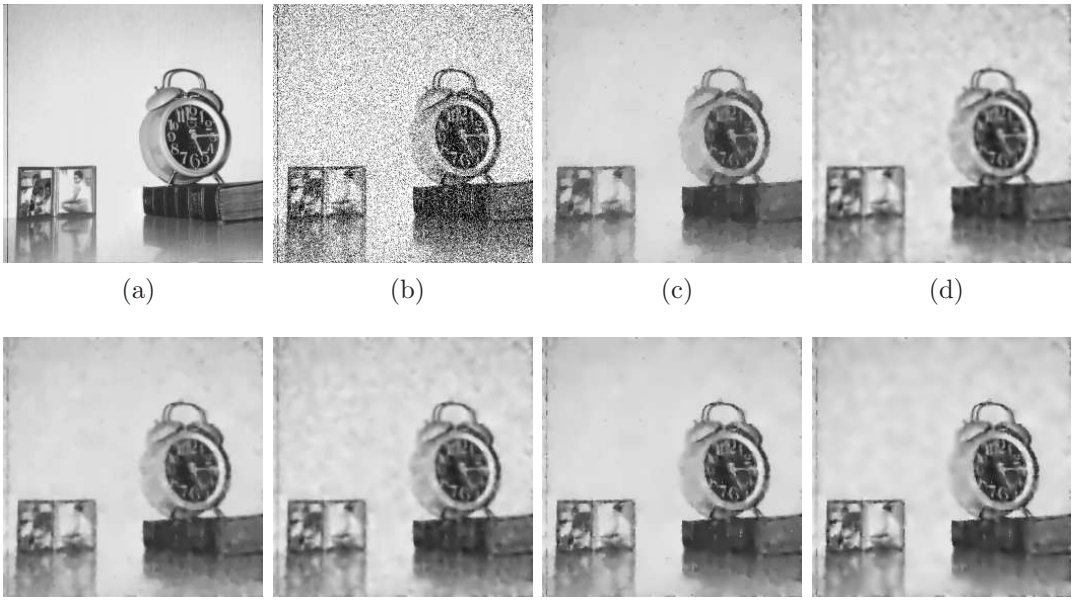

(a) (b) (c) (d)

(e) (f) (g) (h)

Figure 3.9: Comparison of the non-convex hybrid TV with ROF, LLT, and hybrid TV with a high noise level($\sigma = 2.e - 1$). The non-convex hybrid TV improves the SNR value for a wide range of images. (a) Original image (b) Noisy image, (SNR(dB), SSIM) = (2.41, 0.1635) (c) ROF, (SNR(dB), SSIM) = (11.69, 0.8263) (d) LLT, (SNR(dB), SSIM) = (11.76, 0.8139) (e) Hybrid TV with $\alpha_1 = 1, \alpha_2 = 1, g = \frac{1}{2}$, (SNR(dB), SSIM) = (12.01, 0.8418) (f) Hybrid TV with $\alpha_1 = 1, \alpha_2 = 1$, $g =$ edge detection function, (SNR(dB), SSIM) = (11.82, 0.8175) (g) Non-convex hybrid TV with $\alpha_1 = 0.9, \alpha_2 = 0.7, g = \frac{1}{2}$, (SNR(dB), SSIM) = (12.52, 0.8592) (h) Non-convex hybrid TV with $\alpha_1 = 0.9, \alpha_2 = 0.7$, $g =$ edge detection function, (SNR(dB), SSIM) = (12.32, 0.8513)

(a) (b) (c) (d)

(e) (f) (g) (h)

Figure 3.10: Comparison of the non-convex hybrid TV with ROF, LLT, and hybrid TV with a low noise level($\sigma = 7.e-2$). Because the Lena image contains sharp edges, flat regions, as well as slanted regions, the non-convex hybrid TV is well-suited to this image and obtains in the best SNR value. The non-convex hybrid TV achieves higher SNR value than other models for not only a high noise level but also slight noise. (a) Original image (b) Noisy image, (SNR(dB), SSIM) = (8.52, 0.4679) (c) ROF, (SNR(dB), SSIM) = (15.60, 0.8566) (d) LLT, (SNR(dB), SSIM) = (15.89, 0.8615) (e) Hybrid TV with $\alpha_1 = 1, \alpha_2 = 1, g = \frac{1}{2}$, (SNR(dB), SSIM) = (16.18, 0.8725) (f) Hybrid TV with $\alpha_1 = 1, \alpha_2 = 1$, $g =$ edge detection function, (SNR(dB), SSIM) = (16.00, 0.8641) (g) Non-convex hybrid TV with $\alpha_1 = 0.9, \alpha_2 = 0.7, g = \frac{1}{2}$, (SNR(dB), SSIM) = (16.54, 0.8874) (h) Non-convex hybrid TV with $\alpha_1 = 0.9, \alpha_2 = 0.7$, $g =$ edge detection function, (SNR(dB), SSIM) = (16.41, 0.8844)

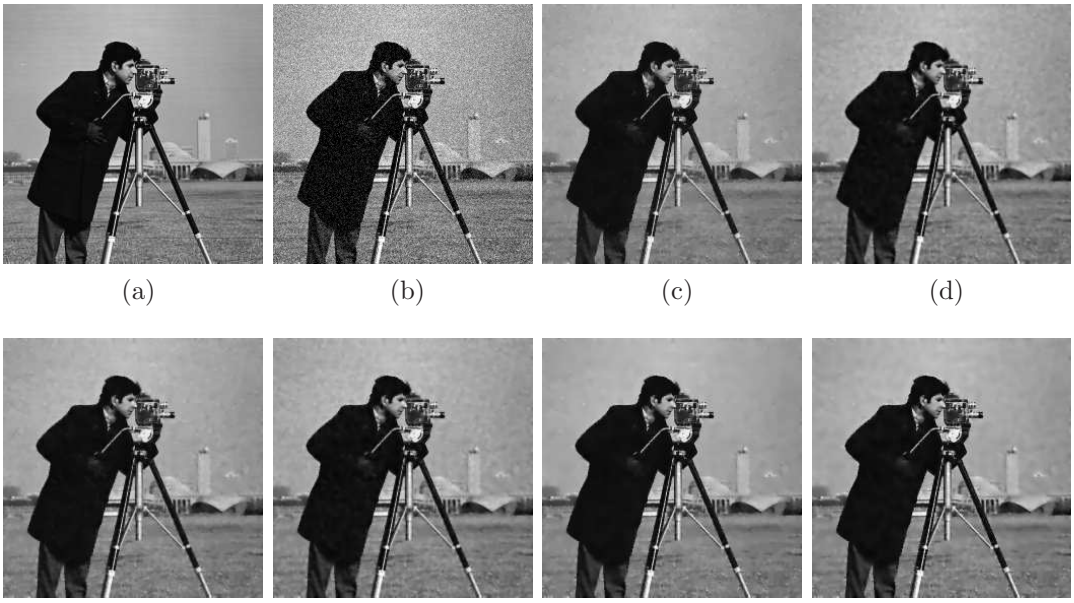

(a) (b) (c) (d)

(e) (f) (g) (h)

Figure 3.11: Comparison of the non-convex hybrid TV with ROF, LLT, and hybrid TV with a low noise level($\sigma = 7.e-2$). The non-convex hybrid TV improves the SNR value for the image that is dominated mainly by piecewise constant regions and sharp edges. (a) Original image (b) Noisy image, (SNR(dB), SSIM) = (11.16, 0.4458) (c) ROF, (SNR(dB), SSIM) = (17.10, 0.8432) (d) LLT, (SNR(dB), SSIM) = (16.76, 0.8303) (e) Hybrid TV with $\alpha_1 = 1, \alpha_2 = 1, g = \frac{1}{2}$, (SNR(dB), SSIM) = (17.20, 0.8496) (f) Hybrid TV with $\alpha_1 = 1, \alpha_2 = 1$, $g =$ edge detection function, (SNR(dB), SSIM) = (17.02, 0.8342) (g) Non-convex hybrid TV with $\alpha_1 = 0.9, \alpha_2 = 0.7, g = \frac{1}{2}$, (SNR(dB), SSIM) = (17.78, 0.8640) (h) Non-convex hybrid TV with $\alpha_1 = 0.9, \alpha_2 = 0.7$, $g =$ edge detection function, (SNR(dB), SSIM) = (17.69, 0.8575)

(a) (b) (c) (d)

Figure 3.12: Comparison of IRHTV and Fergus et al.'s analytic solution for the non-convex anisotropic hybrid TV model ($g = \frac{1}{2}, \alpha_1 = 1$ and $\alpha_2 = \frac{2}{3}$) : (a)Original Image (b) Noisy Image, SNR =-0.15 (c) IRHTV, SNR =11.20 (d) Fergus et al.(Stopping criterion :$(\epsilon, M) = (1.e-4, 100), \gamma = 40$), SNR =11.18

(a) (b) (c)

(d) (e) (f)

Figure 3.13: Comparison between the non-convex hybrid TV and NLTV model (a) Noisy Image (b) NLTV, SNR = 18.04 (c) non-convex hybrid TV , SNR = 18.53 (d) Noisy Image (e) NLTV, SNR = 18.01 (f) non-convex hybrid TV , SNR = 17.46, where $(g, \alpha_1, \alpha_2, M_2) = (\frac{1}{2}, 0.9, 0.7, 10)$

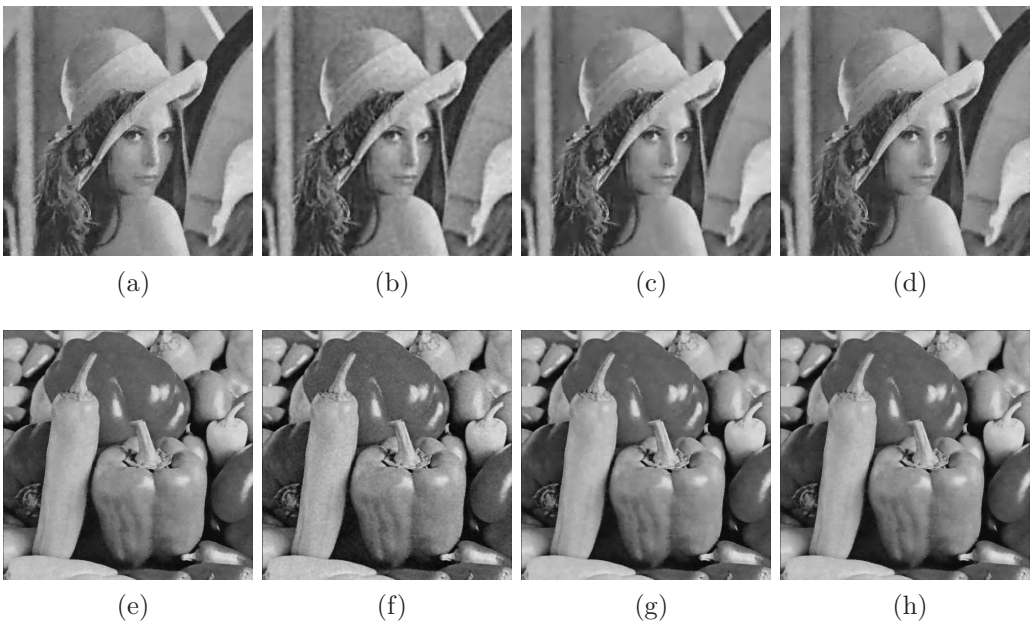

(a) (b) (c) (d)

(e) (f) (g) (h)

Figure 3.14: Comparison between the non-convex hybrid TV and TGV2. (a) ROF, (SNR(dB), Time) = (15.60, 0.16) (b) LLT, (SNR(dB), Time) = (15.89, 0.28) (c) Non-convex hybrid TV with $\alpha_1 = 0.9, \alpha_2 = 0.7, g = \frac{1}{2}$,(SNR(dB), Time) = (16.54, 1.03) (d) TGV^2, (SNR(dB), Time) = (15.72, 0.77) (e) ROF, (SNR(dB), Time) = (17.78, 1.43) (f) LLT, (SNR(dB), Time) = (17.88, 2.78) (g) Non-convex hybrid TV with $\alpha_1 = 0.9, \alpha_2 = 0.7, g = \frac{1}{2}$, (SNR(dB), Time) = (18.65, 9.41) (h) TGV^2, (SNR(dB), Time) = (18.16 , 4.78)

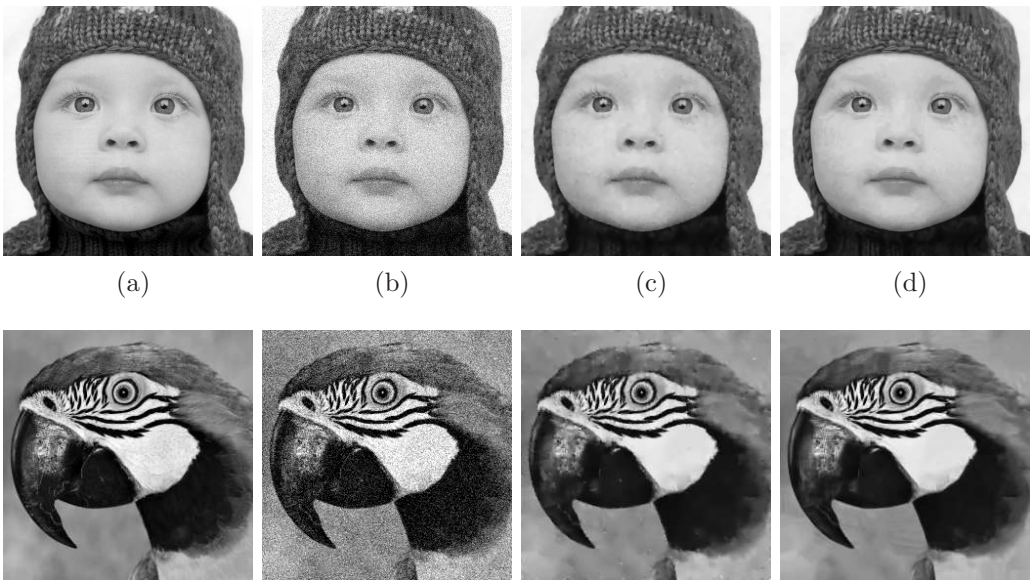

(a) (b) (c) (d)

(e) (f) (g) (h)

Figure 3.15: Comparison between the non-convex hybrid TV and BM3D with a noise level $\sigma = 1.e-1$. (a) Original image (b) Noisy image, (SNR(dB), SSIM) = (9.52, 0.6086) (c) Non-convex hybrid TV with $\alpha_1 = 0.9, \alpha_2 = 0.7, g = \frac{1}{2}$, (SNR(dB), SSIM) = (19.58, 0.8983) (d) BM3D, (SNR(dB), SSIM) = (20.04, 0.9060) (e) Original image (f) Noisy image, (SNR(dB), SSIM) = (8.68, 0.3859) (g) Non-convex hybrid TV with $\alpha_1 = 0.9, \alpha_2 = 0.7, g = \frac{1}{2}$, (SNR(dB), SSIM) = (16.34, 0.8293) (h) BM3D, (SNR(dB), SSIM) = (16.96, 0.8410)

Chapter 4

Image decomposition

In many applications, it is important to control the spatial scale and extract details of an image. Here, we focus on two-scale decomposition. That is, we are interested in decomposing f into two components $f = u + v$, such that u represents a cartoon or geometric (piecewise-smooth) component of f, while v represents the oscillatory or textured component of f. The oscillatory part v should contain essentially the noise and the texture. This chapter is aimed at penalizing the oscillatory components but preserving the structure components.

Two-scale decomposition in an image is classically obtained by applying low-pass and high-pass filters to the given image f, namely $u = LPF(f)$, and the $v = f - u = HPF(f)$. In contrast to the classical Gaussian filter which smooths everywhere equally, there are nonlinear filters such as bilateral filter [68] and WLS filter [32], which preserve edges as well as smooth textures and noises. But, they can not efficiently handle the high contrast textures of the given image. It still remains a hard task to distinguish strong textures and small contrast edges and deal with them appropriately.

In variational approach, a classical decomposition can be achieved by TV minimization model (ROF model) [59] for image denoising. Models where the L^2 norm in the ROF model is substituted by the L^1 norm were suggested. It turns out that TV-L^1 model is well-adapted to preserve geometrical features [19].

But, it is well known that $L_p(\Omega), p \geq 1$ is not small on oscillatory components [1]. It means that TV-L^2 (ROF) and TV-L^1 model do not effectively separate the oscillatory components from the structural components. To overcome this limitation, Meyer [48] proposed weaker norms to replace $\|\cdot\|_{L^2}^2$ in the ROF model, that better model the oscillatory components. He introduced the generalized function spaces $\mathrm{G} = \mathrm{div}(L^\infty) = \dot{W}^{-1,\infty}$, $\mathrm{F} = \mathrm{div}(\mathrm{BMO}) = \dot{\mathrm{BMO}}^{-1}$ and $\mathrm{E} = \dot{B}^{-1}_{\infty,\infty}$ (Besov space). It is motivated by the fact that highly oscillatory signals or images have small norms in G, F or E.

TV-L^2 and the original Meyer's models (TV-div(L^∞), TV-div(BMO), and TV-Besov) have formed the solid foundation for other various researches. But, L^2 norm is not proper for oscillatory components and the norms suggested by Meyer are difficult to compute. Hence, inspired by ROF and Meyer's models, many researches are devoted to design better the fidelity term. As the simple variant of TV-div(L^∞) $= \dot{W}^{-1,\infty}$ model, there is TV-H^{-1}, where $H^{-1} = \dot{W}^{-1,2}$ norm also is small on oscillatory signals.

$$\inf_u J(u) = \int |\nabla u| + \lambda \|f - u\|_{H^{-1}}^2 \tag{4.0.1}$$

As mentioned in section 2.2, TV-Hilbert model is defined using a smoothing kernel K. It is the generalized version of the TV-H^{-1}, since two models are equivalent, when $K = \triangle^{-1}$.

$$\inf_u J(u) = \int |\nabla u| + \lambda \|K * (f - u)\|_{L^2}^2 \tag{4.0.2}$$

By choosing a suitable Hilbert space, it is possible to compute adaptive image decomposition.

Now, we look at this model from different point of view. We denote $g = K * f$. Hence, (4.0.2) can be rewritten by

$$\inf_u J(u) = \int |\nabla u| + \lambda \|K * u - g\|_{L^2}^2 \tag{4.0.3}$$

It's a image deblurring problem, where we desire to recover an original image u from blurred and noisy image g with the given kernel K. So, TV-Hilbert model can be considered as the method that first apply the low-pass filtering with adequate kernel K to f, $g = LPF(f) = K * f$, to remove the oscillatory

component of f, and then deconvolve the given blurred image g in (4.0.3) to restore the geometric component u of original image f. We call it a blur and deblur process.

However, it's limitation is caused by low-pass filtering. Because low-pass filters do not remove only textures but also high-frequency structural information, resulting cartoon part u may show blurry edges. To restore the sharp edges, we deblur the low-pass filtered image g and then, it may lead the staircase artifacts. So there is need for a remedy. To preserve sharp edges and reduce artifacts in deblurring process, we will add a local gradient constraint, which is considered as a local prior in statistical framework. Next section is devoted to design the constraint.

4.1 Local gradient constraint

To suppress ringing artifacts, authors use the blurred image [60] or the flash image [80] to constrain the gradients of the latent image in blind deconvolution problem.

Inspired by the above works, we also use the given image f to restrict the gradients of cartoon component u. This constraint is originated from the fact that the gradients of reconstructed cartoon component u are close to the gradients of the given sharp image f in locally piece-wise smooth regions.

To formulate the local gradient constraint, we build a mask image M using a texture estimator:

$$\mathrm{M} = \begin{cases} 1, & \text{locally piece-wise smooth region;} \\ 0, & \text{locally oscillatory region,} \end{cases}$$

which is described in the following subsection in detail. For all pixels only in locally piece-wise smooth regions, we constrain the cartoon component gradient u to be similar to the given image gradient f. Numerical experiments demonstrate the effect of this constraint in section 4.3. The local gradient constraint clearly helps to preserve the sharp edge and suppress the staircase artifacts.

4.1.1 Texture estimator

To construct a spatially adaptive binary mask image M, we need to design the texture estimator. This local indicator must be built to decide at each point x whether it belongs to a textural region or to a cartoon region. There are several researches [61, 63, 13, 58] to estimate local texture contained in the image.

Su et al. [61] have developed the notion of power map. First, they compute a high-pass version $H = HPF_p(f)$ of the image and then take the absolute value of H. Power map is defined as the local average of this magnitude : $p(f) = G_\sigma * |H|$

Motivated by SSIM [70], Qiegen et al. [58] introduced a novel texture estimator including local variation and structure correlation. When f is a given image and $g = G_\sigma * f$ is a low-pass filtered image, the texture estimator, TD is defined by

$$\begin{aligned} TD(f,g) &= 1 - |c(f,g)s(f,g)| = 1 - \left| \frac{2\sigma_f\sigma_g + k_1}{\sigma_f^2 + \sigma_g^2 + k_1} \frac{\sigma_{fg} + k_2}{\sigma_f\sigma_g + k_2} \right| \\ &= 1 - \left| \frac{2\sigma_{fg} + k_1}{\sigma_f^2 + \sigma_g^2 + k_1} \right| \qquad \text{where} \quad k_2 = k_1/2 \end{aligned} \tag{4.1.1}$$

where $c(f,g) = \dfrac{2\sigma_f\sigma_g + k_1}{\sigma_f^2 + \sigma_g^2 + k_1}$ measures contrast and $s(f,g) = \dfrac{\sigma_{fg} + k_2}{\sigma_f\sigma_g + k_2}$ measures structure. σ_f denotes $\left(\sum_{i=1}^{N} w_i (f_i - \mu_f)^2 \right)^{\frac{1}{2}}$ where $\mu_f = \sum_{i=1}^{N} w_i f_i$ and σ_{fg} denotes $\sum_{i=1}^{N} w_i (f_i - \mu_f)(g_i - \mu_g)$. TD ranges from 0 to 1 and the value is increasing as a pixel belongs to oscillatory regions.

To estimate the local amount of texture, there are texture estimators [63, 13] using the local total variation. In [63], authors observed that if a pixel corresponds to a locally texture region, the average value in the small neighborhood is higher than that in the large neighborhood image. They proposed the local total variation T defined by

$$T_{\sigma_1,\sigma_2}(\nabla f) = \frac{G_{\sigma_1} * \|\nabla f\|}{G_{\sigma_2} * \|\nabla f\|} n(\|\nabla f\|) \tag{4.1.2}$$

where $\sigma_1 < \sigma_2$ and $n(\cdot)$ is a function to control noises. Hence, if the image is locally textured, corresponding value T is bigger than 1.

Buades et al. [13] approached the issue in a quite different way. They defined the local total variation (LTV) at x

$$LTV_\sigma(f)(x) = G_\sigma * |\nabla f|(x)$$

and the relative reduction rate of LTV

$$\lambda_\sigma(x) := \frac{LTV_\sigma(f)(x) - LTV_\sigma(G_\sigma * f)(x)}{LTV_\sigma(f)(x)}.$$

These definitions originated from the observation that when a low-pass filter G_σ is applied to the image f, the LTV of texture and cartoon components behave differently. Moreover, we can figure out the local oscillatory behavior of function f from the relative reduction rate of LTV and, finally we can classify pixel into two categories based on this rate. If a pixel belongs to a texture region, then reduction is significantly increased, the corresponding value λ_σ is close to 1.

To demonstrate the different behavior of the relative reduction rate of LTV for a pixel, we display the plot of $\lambda_\sigma(x)$ for several pixels. In Figure 4.1, one is a blue dot corresponding to a pixel on an edge, another is a green circle corresponding to a pixel on a texture region, and the other is a red square corresponding to a pixel on a homogeneous region. We observed that as a scale σ increases, $\lambda_\sigma(x)$ for a pixel which belongs to oscillatory pattern quickly increases to get quite near to value one. On the other hand, $\lambda_\sigma(x)$ on a edge or homogeneous region rises gradually and does not exceed, roughly speaking, 0.5.

To illustrate the effect of different low-pass filters, we applied L_σ and the sharper kernel K_σ to the given image. The filtered image $\hat{u} = \hat{L_\sigma}\hat{f}$, where $\widehat{L_\sigma}(\xi) = \frac{1}{1+(2\pi\sigma|\xi|)^4}$ is a solution in Fourier of H^1-H^{-1} model,

$$\min_u \left\{ \int |\nabla u|^2 + \lambda \|f - u\|^2_{H^{-1}} \right\} \tag{4.1.3}$$

where $\lambda = \frac{1}{\sigma^4}$. Since K_σ, corresponding to $\widehat{K_\sigma}(\xi) = \exp\{-(2\pi\sigma|\xi|)^4\}$, behaves like the characteristic function, it is considered as a sharper kernel than L_σ.

But we observed that the plots of λ_σ corresponding two different kernels are nearly similar. This comparison shows that the relative reduction rate of LTV of texture and cartoon components behaves differently, irrespective of the choice of a low-pass filter.

(a) Original image

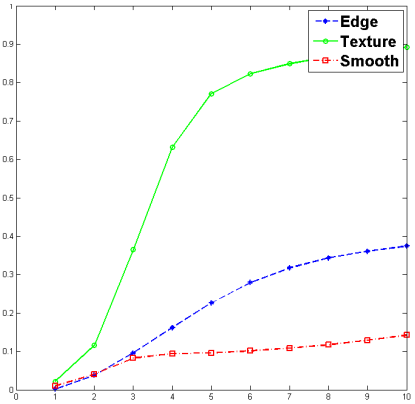

(b) L_σ : $\widehat{L_\sigma}(\xi) = \frac{1}{1+(2\pi\sigma|\xi|)^4}$

(c) Original image

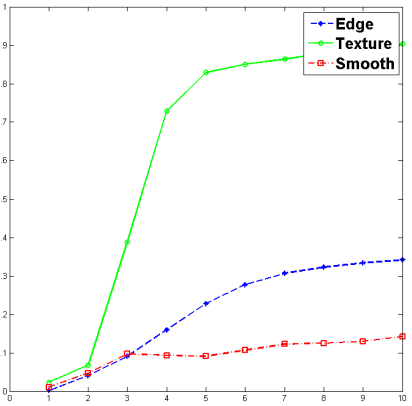

(d) K_σ: $\widehat{K_\sigma}(\xi) = \exp\{-(2\pi\sigma|\xi|)^4\}$

Figure 4.1: Plot of $\lambda_\sigma(x)$ for pixels. To illustrate the effect of different low-pass filters, we applied the sharper kernel K_σ instead of L_σ to the given image.

However, the decomposition solutions highly depend on the selection of the σ value of the low-pass filter G_σ, since this value is related to the scale of

texture. To obtain the best solution, we need a properly tuned σ according to the scale of a given image.

Based on these texture estimators, we construct a binary mask M and use this matrix to constrain the gradients of the cartoon component u. To build the mask M, we must set the threshold value t properly. If the texture estimator value for a pixel is larger than the threshold, then we regard this pixel as in locally textured regions. Conversely, if the value is smaller than the threshold, corresponding pixel is in locally piece-wise smooth region Ω, which is shown as a set of all white pixels.

$$\mathrm{M} = \begin{cases} 1, & \text{in region } \Omega; \\ 0, & \text{in region } \Omega^c. \end{cases}$$

For all pixels in Ω, we restrict the BV components gradient close to the given image gradient.

Figure 4.2 displays two texture estimators. Figure 4.2b and 4.2c are corresponding to λ_σ and TD, which were proposed in [13] and [58] respectively. Since TD uses a Gaussian kernel and we desire a fair comparison, we adopt the same kernel for λ_σ. We observed that both λ_σ and TD are small on edges and smooth regions but are large on oscillatory regions. Figure 4.2e and 4.2f show the binary mask M constructed by a properly tuned threshold value t. Two results are similar and classify a pixel into two categories properly.

4.2 The proposed model

Simply speaking, the proposed model consists of the blur and deblur process. First, we apply a low-pass filter to the given image f to remove the texture and noise. But, low-pass filtering does remove not only oscillatory components but also structure informations, to result in blurred edges: see Figure 4.2a and Figure 4.2d. Thus, we do deconvolve the low-pass filtered image g by introducing a local gradient constraint. The deblurring model is represented as follows :

$$\min_u \|\nabla u\|_p + \frac{\nu}{2}\|M \cdot (\nabla u - \nabla f)\|_2^2 + \frac{\mu}{2}\|g - K * u\|_{L^q}^q \tag{4.2.1}$$

where M is the binary mask image and $\cdot$ means the element-wise multiplication. To measure the difference between the gradient of the restored image

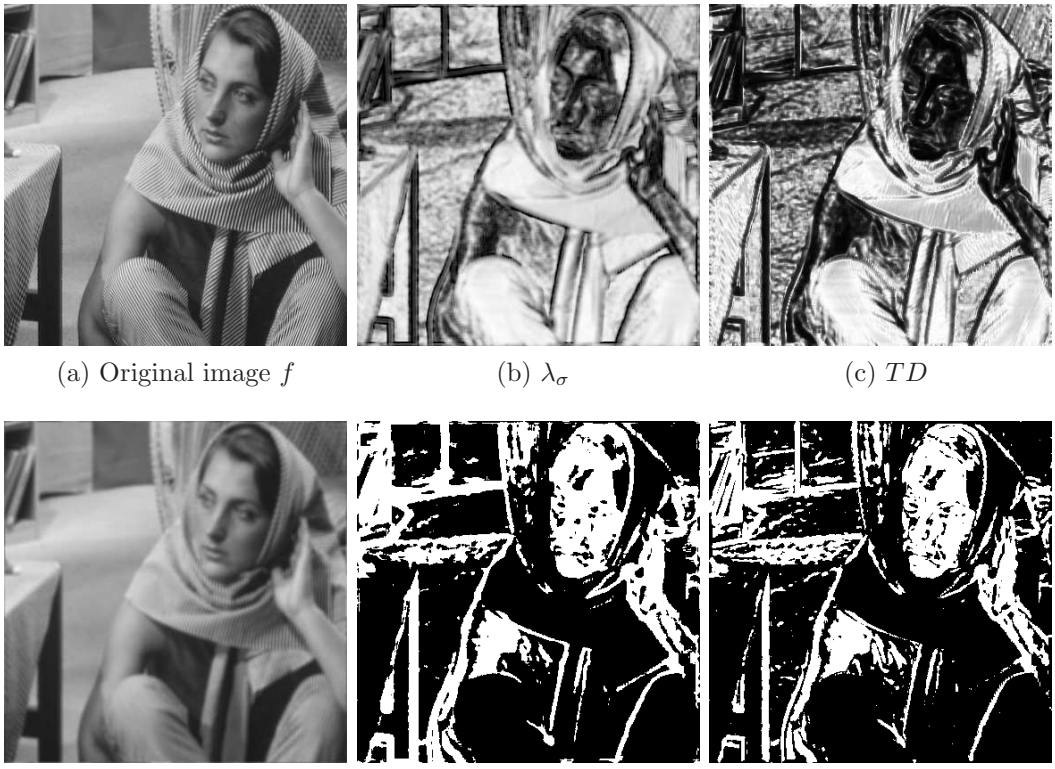

(a) Original image f (b) λ_σ (c) TD

(d) Low-pass filtered image g (e) M_{λ_σ} (f) M_{TD}

Figure 4.2: Texture estimator and binary mask M using the low-pass filtered image $g = G_\sigma * f$. (a) Original image (b) The relative reduction rate of LTV :λ_σ ([13]) (c) TD ([58]) (d) Low-pass filtered image (Gaussian kernel, $\sigma = 3$). (e) Binary mask M_{λ_σ} using (b) and hard thresholding value $t = 0.5$ (f) Binary mask M_{TD} using (c) and hard thresholding value $t = 0.25$

u and the gradient of the given image f, we adopt the cost function ρ. Zhuo et. al [80] use the robust estimate function $\rho(x) = \frac{1}{2}\log(1 + \frac{1}{2}(\frac{x}{\epsilon})^2)$ to reject outliers and noises. For the sake of simplicity, we can use $\rho(x) = \frac{1}{2}x^2$ and then derive the second term in (4.2.1). Outside of Ω where $M(x) = 0$, the value of ∇f is unused and u is only influenced by the regularizer term $\|\nabla u\|_p$ and the fidelity term $\frac{\mu}{2}\|g - K * u\|_{L^q}^q$. That is, (4.2.1) is identical to TV-Hilbert model. However, for all pixels in Ω, the second term of (4.2.1) is activated and then, (4.2.1) can enforce the cartoon components u gradient to be close

to the given image f gradient.

After the above process, we obtain the geometric components u from the blurred image g, and we get the oscillatory components $v = f - u$.

Following subsections are devoted to optimize (4.2.1) by using advanced optimization technique. Instead of directly solving (4.2.1), we use the well-known variable-splitting and penalty techniques [71] to handle this challenging problem efficiently.

4.2.1 Algorithm : Anisotropic TV-L^2

In this subsection, we will describe that the variable splitting and penalty method can be used to solve this problem (4.2.1). As it is well known in [71, 60, 74], it is not only simple but also significantly efficient. We follow their direction.

First, we consider anisotropic TV and L^2 fidelity, $\|\nabla u\|_1 = \sum_i |(u_x)_i| + |(u_y)_i|$.

$$\min_u \|\nabla u\|_1 + \frac{\nu}{2}\{\|M_x \cdot (\nabla_x u - \nabla_x f)\|_2^2 + \|M_y \cdot (\nabla_y u - \nabla_y f)\|_2^2\} + \frac{\mu}{2}\|g - K * u\|_2^2 \tag{4.2.2}$$

To apply a variable-splitting, we first substitute $\nabla_x u$ and $\nabla_y u$ by d_x and d_y respectively. This yields the constrained problem

$$\begin{aligned} \min_u \quad & |d_x| + |d_y| + \frac{\nu}{2}\{\|M_x \cdot (d_x - \nabla_x f)\|_2^2 + \|M_y \cdot (d_y - \nabla_y f)\|_2^2\} + \frac{\mu}{2}\|g - K * u\|_2^2 \\ \text{s.t.} \quad & d_x = \nabla_x u \text{ and } d_y = \nabla_y u \end{aligned}$$

By introducing quadratic penalty function terms, we convert this formulation into an unconstrained problem.

$$\begin{aligned} \min_{d_x, d_y, u} \quad & |d_x| + |d_y| + \frac{\nu}{2}\{\|M_x \cdot (d_x - \nabla_x f)\|_2^2 + \|M_y \cdot (d_y - \nabla_y f)\|_2^2\} \\ & + \frac{\mu}{2}\|g - K * u\|_2^2 + \frac{\lambda}{2}\|d_x - \nabla_x u\|_2^2 + \frac{\lambda}{2}\|d_y - \nabla_y u\|_2^2 \end{aligned} \tag{4.2.3}$$

where λ is a weight parameter whose value controls how strongly d_x and d_y are constrained to be close to $\nabla_x u$ and $\nabla_y u$. As well known, the penalty parameter λ goes to infinity for the convergence of the quadratic penalty

method. But it is difficult to determine how sufficiently large λ value must be. And the convergence speed may be slow for too large λ. So, we need to adjust the value of λ adaptively. In this work, we use the continuation scheme [71, 60, 74] to accelerate the speed of convergence. The value of λ is automatically adapted in each iteration. Initially starting a small value λ_0, its value will gradually increase to the final value λ_{max} by being multiplied by κ time. In all experiments, we set $\lambda_0 = 2^0$ and $\lambda_{max} = 2^{10}$.

The basic idea of these algorithms [71, 60, 74] is to split the L_1 and L_2 components of the functional. The object functional in (4.2.3) is quadratic u and separable in d, so it is computationally tractable. Hence, we apply the splitting scheme, and perform iterative minimization efficiently with respect to u and d. Iterative minimization scheme is composed of two steps: u-subproblem and d-subproblem.

The first subproblem we solve with fixed d is

$$u^{k+1} = \min_u \frac{\mu}{2}\|g - K * u\|_2^2 + \frac{\lambda}{2}\|d_x - \nabla_x u\|_2^2 + \frac{\lambda}{2}\|d_y - \nabla_y u\|_2^2 \qquad (4.2.4)$$

which has the optimality condition

$$(\mu K^\top K - \lambda\triangle)u^{k+1} = \mu K^\top g + \lambda\nabla_x^\top d_x^k + \lambda\nabla_y^\top d_y^k \qquad (4.2.5)$$

In the second subproblem, we fix u and compute the optimal value d_x and d_y respectively.

$$d_x^{k+1} = \min_{d_x} |d_x| + \frac{\nu}{2}\|M_x \cdot (d_x - \nabla_x f)\|_2^2 + \frac{\lambda}{2}\|d_x - \nabla_x u\|_2^2,$$

Fortunately, there is no coupling between elements of d. So, each pixel is minimized separately. We can simplify this formulation using 1 dimensional shrinkage operator and explicitly compute the optimal value of d_x.

$$(d_x)_i^{k+1} = shrink_{1D}\left(\frac{\nu(M_x)_i(\nabla_x f)_i + \lambda(\nabla_x u)_i}{\nu(M_x)_i + \lambda}, \frac{1}{\nu(M_x)_i + \lambda}\right) \qquad (4.2.6)$$

where

$$shrink_{1D}(x, \gamma) = \max(|x| - \gamma, 0) * \frac{x}{|x|}$$

Similarly, we can compute the optimal value of d_y as follows

$$(d_y)_i^{k+1} = shrink_{1D}\left(\frac{\nu(M_y)_i(\nabla_y f)_i + \lambda(\nabla_y u)_i}{\nu(M_y)_i + \lambda}, \frac{1}{\nu(M_y)_i + \lambda}\right) \tag{4.2.7}$$

If we choose the robust estimate function $\rho(x) = \int \log\left(1 + \frac{1}{2}(\frac{x}{\epsilon})^2\right)$, we must develop iterative reweighted type algorithm as done in [80]. Finally, if we plug this problem into continuation scheme on the penalty parameter λ with a warm start for a complete algorithm, we get the alternative minimization algorithm for the anisotropic TV and L^2 functional:

Algorithm 5 :
Anisotropic TV-L^2 deblurring with local gradient constraint

Initialization: $u^0 = f,\ \lambda = \lambda_0$
While $\lambda \leq \lambda_{max}$
  While $\|u^k - u^{k-1}\|_2 > tol$
    $d_x^{k+1} = shrink_{1D}\left(\frac{\nu M_x \cdot \nabla_x f + \lambda \nabla_x u^k}{\nu M_x + \lambda}, \frac{1}{\nu M_x + \lambda}\right)$
    $d_y^{k+1} = shrink_{1D}\left(\frac{\nu M_y \cdot \nabla_y f + \lambda \nabla_y u^k}{\nu M_y + \lambda}, \frac{1}{\nu M_y + \lambda}\right)$
    $(\mu K^\top K - \lambda \triangle) u^{k+1} = \mu K^\top g + \lambda \nabla_x^\top d_x^{k+1} + \lambda \nabla_y^\top d_y^{k+1}$
  end
  $\lambda \leftarrow \lambda * \kappa$
end

4.2.2 Algorithm : Isotropic TV-L^2

Now, we consider the isotropic TV as a regularizer and L^2 fidelity.

$$\min_u \|\nabla u\|_2 + \frac{\nu}{2}\|M \cdot (\nabla u - \nabla f)\|_2^2 + \frac{\mu}{2}\|g - K * u\|_2^2 \tag{4.2.8}$$

where $\|\nabla u\|_2 = \sum_i \sqrt{(\nabla_x u)_i^2 + (\nabla_y u)_i^2}$.
By introducing the set of auxiliary variables $d = (d_x, d_y)$ for ∇u, the formulation of the above problem then becomes

$$\begin{aligned}\min_{d_x, d_y, u} \quad & \|(d_x, d_y)\|_2 + \frac{\nu}{2}\{\|M \cdot (d_x - \nabla_x f)\|_2^2 + \|M \cdot (d_y - \nabla_y f)\|_2^2\} \\ & + \frac{\mu}{2}\|g - K * u\|_2^2 + \frac{\lambda}{2}\|d_x - \nabla_x u\|_2^2 + \frac{\lambda}{2}\|d_y - \nabla_y u\|_2^2\end{aligned}$$

where $\|(d_x, d_y)\|_2 = \sum_i \sqrt{(d_x)_i^2 + (d_y)_i^2}$.

In order to apply the iterative minimization procedure to this problem, we must solve the d subproblem

$$\begin{aligned}(d_x, d_y) = \min_{d_x, d_y} \quad & \|(d_x, d_y)\|_2 + \frac{\nu}{2}\{\|M \cdot (d_x - \nabla_x f)\|_2^2 + \|M \cdot (d_y - \nabla_y f)\|_2^2\} \\ & + \frac{\lambda}{2}\|d_x - \nabla_x u\|_2^2 + \frac{\lambda}{2}\|d_y - \nabla_y u\|_2^2 \end{aligned} \tag{4.2.9}$$

Even though we do not decouple the d_x and d_y variables as we did in the anisotropic case, we can still explicitly solve the minimization problem for (d_x^{k+1}, d_y^{k+1}). The solution of (4.2.9) is given by a generalized shrinkage formula defined in [71]:

$$\begin{aligned} d^{k+1} &= shrink\left(\frac{\nu M \cdot \nabla f + \lambda \nabla u^k}{\nu M + \lambda}, \frac{1}{\nu M + \lambda}\right) \\ &= \max\left(\|\frac{\nu M \cdot \nabla f + \lambda \nabla u}{\nu M + \lambda}\|_2 - \frac{1}{\nu M + \lambda}, 0\right) \frac{\frac{\nu M \cdot \nabla f + \lambda \nabla u^k}{\nu M + \lambda}}{\|\frac{\nu M \cdot \nabla f + \lambda \nabla u^k}{\nu M + \lambda}\|_2} \end{aligned} \tag{4.2.10}$$

The u-subproblem is the same as that of the anisotropic TV-L^2 deblurring in previous subsection. Similarly, we derive our alternating minimization algorithm, which is summarized in Algorithm 6.

Algorithm 6:
Isotropic TV-L^2 deblurring with local gradient constraint

Initialization: $u^0 = f,\ \lambda = \lambda_0$
While $\lambda \leq \lambda_{max}$
  While $\|u^k - u^{k-1}\|_2 > tol$
    $d^{k+1} = shrink\left(\frac{\nu M \cdot \nabla f + \lambda \nabla u^k}{\nu M + \lambda}, \frac{1}{\nu M + \lambda}\right)$
    $(\mu K^\top K - \lambda \triangle) u^{k+1} = \mu K^\top g + \lambda \nabla_x^\top d_x^{k+1} + \lambda \nabla_y^\top d_y^{k+1}$
  end
  $\lambda \leftarrow \lambda * \kappa$
end

4.2.3 Algorithm : Isotropic TV-L^1

In [36], when texture-like natural images are convolved with compact averaging kernels with zero mean, they have statistically Laplacian probability distributions. For image decomposition, the texture part v on a suitable compact set has zero mean. Therefore, we consider the model (4.2.1) with $q = 1$.

$$\min_u \|\nabla u\|_2 + \frac{\nu}{2}\|M \cdot (\nabla u - \nabla f)\|_2^2 + \frac{\mu}{2}\|K * u - g\|_1^1 \tag{4.2.11}$$

Let us apply the variable substitution and penalty method to the above problem (4.2.11). To split L_1 and L_2 terms efficiently, we introduce two auxiliary variables $d = (d_x, d_y)$ and e. The transformed formulation is as follows:

$$\begin{aligned}\min_{d_x,d_y,e,u} \quad & \|d\|_2 + \frac{\nu}{2}\{\|M \cdot (d_x - \nabla_x f)\|_2^2 + \|M \cdot (d_y - \nabla_y f)\|_2^2\} + \frac{\mu}{2}\|e\|_1 \\ & + \frac{\lambda}{2}\|d_x - \nabla_x u\|_2^2 + \frac{\lambda}{2}\|d_y - \nabla_y u\|_2^2 \\ & + \frac{\tau}{2}\|e - (K * u - g)\|_2^2 \end{aligned} \tag{4.2.12}$$

To make the problem easier to tackle, we use the splitting scheme to (4.2.12) and then, derive three subproblems : u-subproblem, d-subproblem, e-subproblem We minimize each subproblem alternatively.

First, we consider u-subproblem.

$$u^{k+1} = \min_u \frac{\lambda}{2}\|d_x - \nabla_x u\|_2^2 + \frac{\lambda}{2}\|d_y - \nabla_y u\|_2^2 + \frac{\tau}{2}\|K * u - g - e\|_2^2 \tag{4.2.13}$$

From optimality condition, we derive the following system :

$$(\tau K^\top K - \lambda \triangle)u^{k+1} = \lambda \nabla_x^\top d_x^k + \lambda \nabla_y^\top d_y^k + \tau K^\top (g + e) \tag{4.2.14}$$

As the case of the subsection 4.2.2, we use the generalized shrinkage formula to obtain d_x and d_y, which is corresponding (4.2.10).

Finally, in order to get e, we solve the e-subproblem.

$$e^{k+1} = \min_e \frac{\mu}{2}\|e\|_1 + \frac{\tau}{2}\|e - (K * u - g)\|_2^2$$

Using a 1D shrinkage operator (4.2.1), we can explicitly compute the optimal value of e.

$$e_i^{k+1} = shrink_{1D}\left((K * u)_i - g_i, \frac{\mu}{2\tau}\right) \tag{4.2.15}$$

Now, we obtain the alternating minimization algorithm for the isotropic TV and L^1 functional:

Algorithm 7 :
Isotropic TV-L^1 deblurring with local gradient constraint

Initialization: $u^0 = f,\ \lambda = \lambda_0$
While $\lambda \leq \lambda_{max}$
  While $\|u^k - u^{k-1}\|_2 > tol$
    $d^{k+1} = shrink\left(\frac{\nu M \cdot \nabla f + \lambda \nabla u^k}{\nu M + \lambda}, \frac{1}{\nu M + \lambda}\right)$
    $e^{k+1} = shrink_{1D}(K * u^k - g, \frac{\mu}{2\tau})$
    $(\tau K^\top K - \lambda \triangle) u^{k+1} = \lambda \nabla_x^\top d_x^{k+1} + \lambda \nabla_y^\top d_y^{k+1} + \tau K^\top (g + e^{k+1})$
  end
    $\lambda \leftarrow \lambda * \kappa$
end

4.3 Numerical experiments and discussion

To demonstrate the effectiveness of our model, we compare it against other models. One is the TV-Hilbert model that stands for TV-X type models. To implement of the TV-Hilbert model, we use the split Bregman method [34]. The other is BLMV filter [13], which is considered as a typical nonlinear filter. We use the online demo, which is available in
http://demo.ipol.im/demo/blmv_nonlinear_cartoon_texture_decomposition/.

And, we do the comparison between isotropic TV and anisotropic TV, and between L^2 and L^1 fidelity in the proposed models. In Figure 4.3, images tested in all numerical experiments are displayed.

First, we compare between the TV-Hilbert model and the proposed model to observe the effect of local gradient constraint in Figure 4.4, To be a fair comparison, we use the same low-pass filter $\widehat{K_\sigma}(\xi) = \exp -(2\pi\sigma|\xi|)^4$ and choose isotropic TV and L^2 fidelity term for both models. To decompose the texture from the images, we can design various texture-specific kernel K for TV-Hilbert model. For example, there are $K = I$ corresponding to the ROF

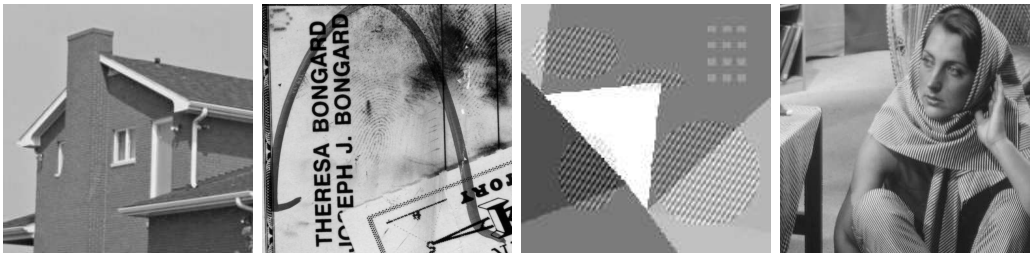

(a) House (b) Fingerprint (c) Diagram (d) Barbara

Figure 4.3: Test images

model [59], $K = -\triangle^{-1}$ corresponding to the OSV model [54] and $K =$ Gabor filter corresponding to the TV-Gabor model [5]. Because of its simplicity, we shall retain this version (4.0.2) of TV-Hilbert model in the experiments after fixing adequately the kernel K. If we choose a different kernel, numerical results will be slightly different but not significantly.

We choose the reduction ratio of LTV, λ_σ as a texture estimator to build the binary mask M of our model. For λ_σ, we use the same kernel K as low-pass filter for consistency. As seen in Figure 4.2, the difference in performance among texture estimators is not great. So we adopt the reduction ratio of LTV λ_σ as a texture estimator unless otherwise noted.

The choice of hard threshold value t is critical for building a binary mask based on the texture estimator. According to the threshold value, a pixel may be confirmed to belong to a cartoon side, which is permitted to keep the gradient. Or, depending on this value, it may be proven to be on a oscillatory side, which finally is smoothed. But, ultimately, we want to reduce the number of parameters of algorithm to obtain a simple method. So, it seems advisable to fix the threshold value. We set $t = 0.25$ in all experiments. Of course, changes in the threshold value may have a influence on decomposition results. But numerical results show that the chosen value is reasonable.

The choice of parameter μ in both TV-Hilbert and the proposed model is critical. Its value controls the amount of regularization and is related the texture scale σ of the low-pass filter K_σ. To observe the effect of μ, we fix the texture scale σ in the low-pass filter and only change the value of μ in Figure 4.4. As the μ value increases from 10 to 1000, eventually, the structural

components such as edges go into the cartoon part.

To demonstrate the local gradient constraint, we display the results of both the TV-Hilbert model and the proposed model. First and second columns correspond to the TV-Hilbert model and third and fourth columns correspond to our model. Our model successfully separates the given image into cartoon and texture components. However, in TV-Hilbert model, a considerable amount of edges remains in texture side to cause blurry edges in cartoon side.

In following other figures, we can also observe the effect of the local gradient constraint, where that our model is superior to the TV-Hilbert model is illustrated for all cases : isotropic TV-L^2, anisotropic TV-L^2 and isotropic TV -L^1. Figure 4.5 shows that the TV-Hilbert model decomposes not only fingerprint but also the edges of texts into oscillatory components, but our model does keep well the edges on cartoon components. In Figure 4.6, we observe that the face of Barbara in our model is more natural than the TV-Hilbert model. In our model, the stair-case artifacts on her face disappear.

From Figure 4.5 to Figure 4.7, we compare the proposed models with BLMV filter [13]. In Figure 4.5 and Figure 4.6, the visual difference between the nonlinear filter and the proposed models is not significant. However, the superiority of our model to the BLMV filter is clearly demonstrated in Figure 4.7. Although the scale σ has been tuned, BLMV filter yields poor results. For small σ, this filter cannot separate the texture pattern from cartoon components. As σ increases, small blocks in upper right corner as well as oscillatory patterns go into texture side. Moreover, blurry edges and blocky artifacts appear in cartoon components. Our models, on the other hand, produce better results than the TV-Hilbert model as well as the BLMV filter. In TV-Hilbert models, small blocks in upper right corner go into texture components and at triple junctions the broken edges appear. However, by adding local constraint, our models compensate these drawbacks and improve separation results. Especially, isotropic TV-L^2 yields the best decomposition results. For anisotropic TV-L^2 case, there are features that remains common in both TV-Hilbert model and our model. They keep the small block in upper right corner on cartoon side and preserve sharp edges for blocks. But there are aliasing artifacts. These artifacts are also displayed on the scarf; see

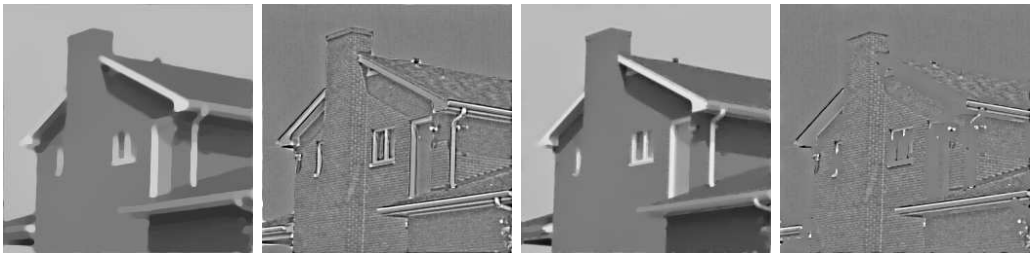

(a) TV-Hilbert model : $\mu = 10$ (b) The proposed model : $\mu = 10$

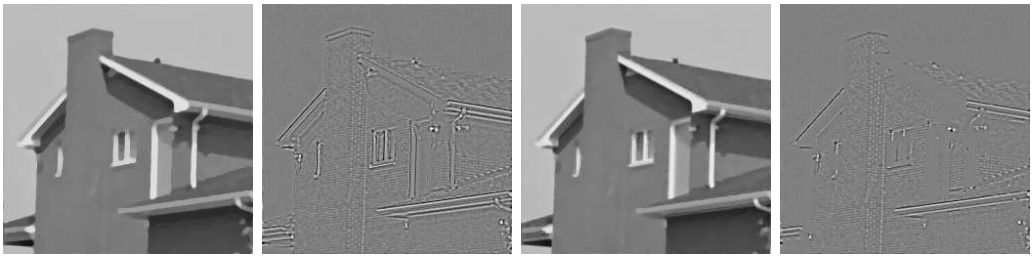

(c) TV-Hilbert model : $\mu = 100$ (d) The proposed model : $\mu = 100$

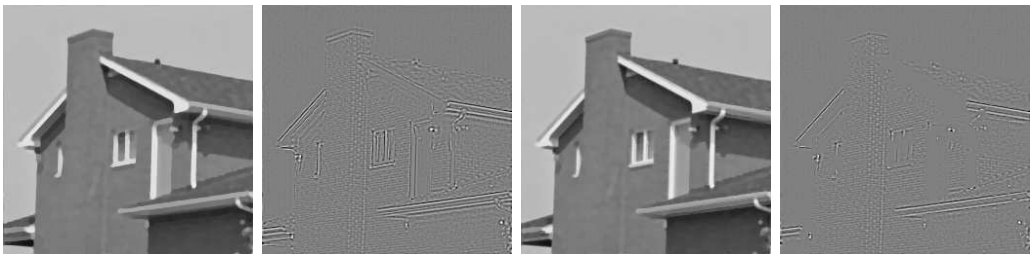

(e) TV-Hilbert model : $\mu = 1000$ (f) The proposed model : $\mu = 1000$

Figure 4.4: To demonstrate the effect of local gradient constraint, we do comparison between the TV-Hilbert model and proposed model. The first and second columns correspond to the TV-Hilbert model (without a local constraint) and the third and fourth columns correspond to the proposed model with additional local gradient constraint. From top row to bottom row, μ increases as it is noted. For a fair comparison, we use the same kernel K_σ in these all experiments, and adopt isotropic TV and L^2 fidelity.

Figure 4.6d. For all cases in our models, we can make sure of the improvement over other models.

We have considered the TV-Hilbert model as a blur and deblur process for the image decomposition problem. By incorporating additional local constraint of image gradient into the classical TV-Hilbert model, we derived more efficient image decomposition results. The proposed model can separate texture regions v from the given image f effectively while it can preserve the sharp edges and keep homogeneous regions in structural components u. We have studied the effect of the local gradient constraint and illustrated that with numerical examples.

There is no unique decomposition of an image into two-scale : cartoon and texture. At close range, a texture may be just a set of well-structured objects. Thus, it can be kept in the cartoon part or the textural part according to the scale parameter. The scale parameter that must be chosen by the user is therefore crucial and indispensable. But, in the current research, there remain several parameters which must be chosen properly for each image. How to reduce its parameters freedom for constructing a general decomposition model is a future research direction. To design a texture-specific kernel is an interesting issue.

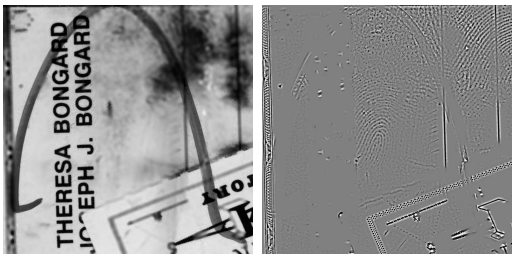

(a) BLMV

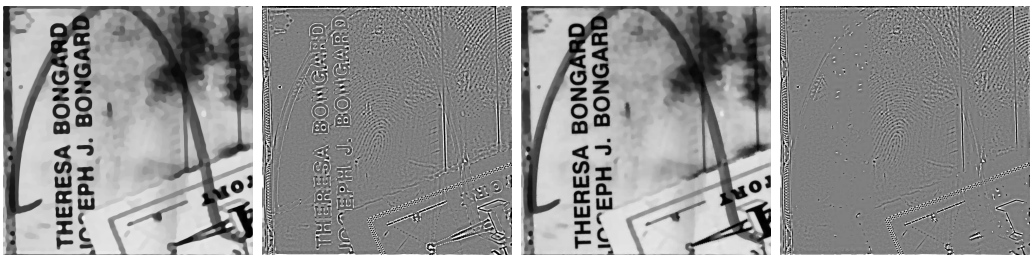

(b) Isotropic TV + L2

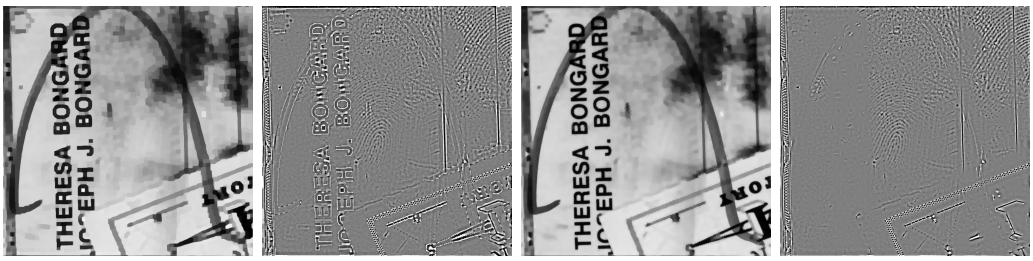

(c) Anisotropic TV + L2

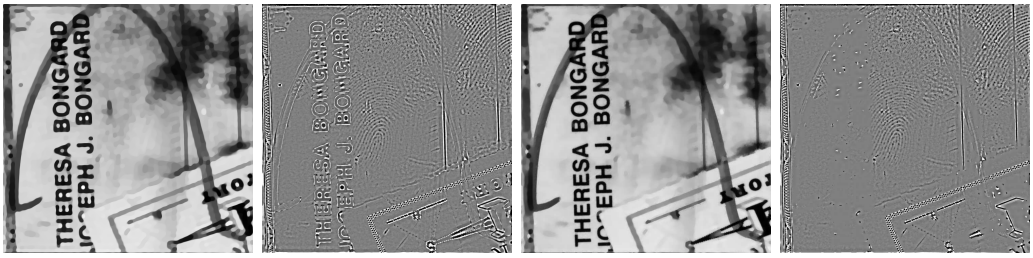

(d) Isotropic TV + L1

Figure 4.5: The first row corresponds to the BLMV filter. From the second to fourth row, the first and second columns correspond to the TV-Hilbert model and the third and fourth columns correspond to the proposed model. For a fair comparison, we use the same kernel K_σ and fix μ value.

(a) BLMV, $\sigma = 2.5$ (b) BLMV, $\sigma = 3.5$

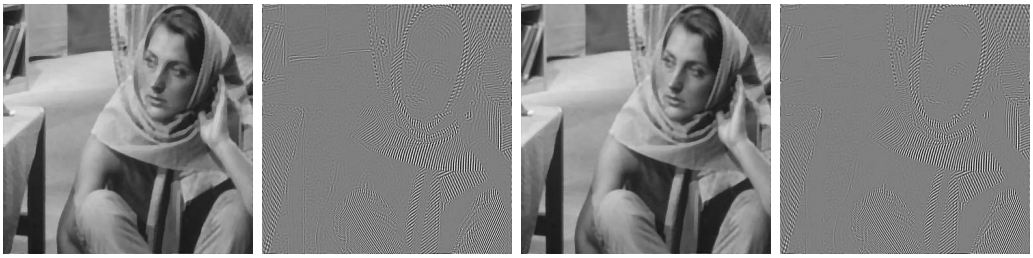

(c) Isotropic TV + L2

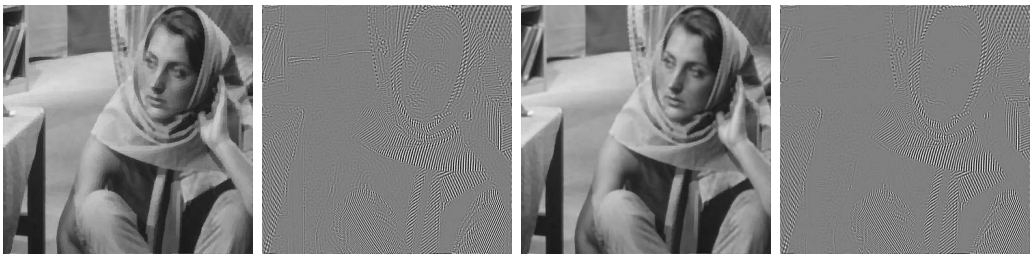

(d) Anisotropic TV + L2

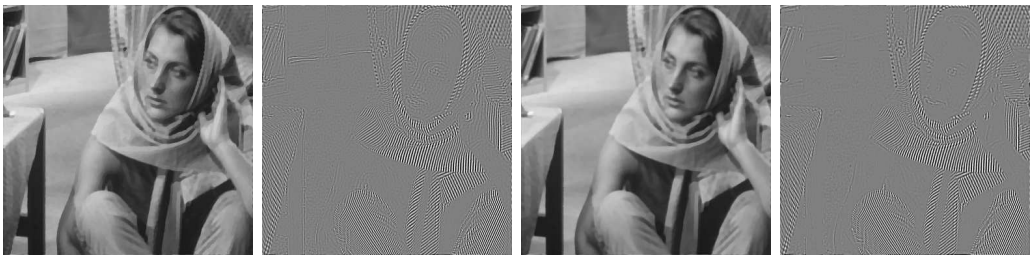

(e) Isotropic TV + L1

Figure 4.6: The first row corresponds to the BLMV filter. Two different σ values are used as it is noted. From the second to fourth row, the first and second columns correspond to the TV-Hilbert model and the third and fourth columns correspond to the proposed model. For a fair comparison, we use the same kernel K_σ and fix μ value.

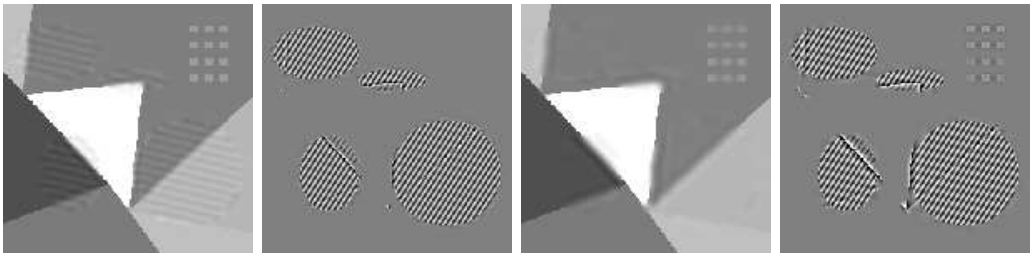

(a) BLMV, $\sigma = 2$ (b) BLMV, $\sigma = 3$

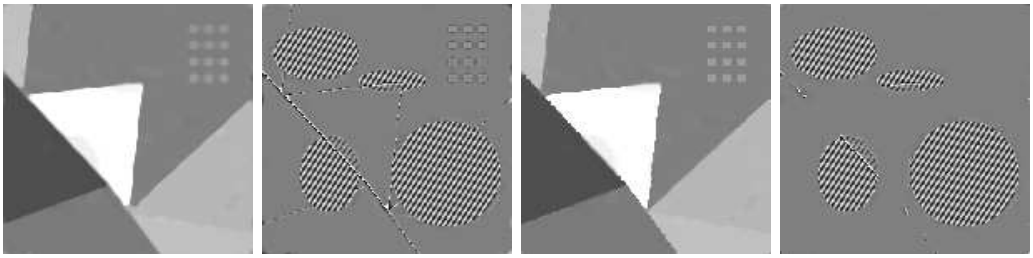

(c) Isotropic TV + L2

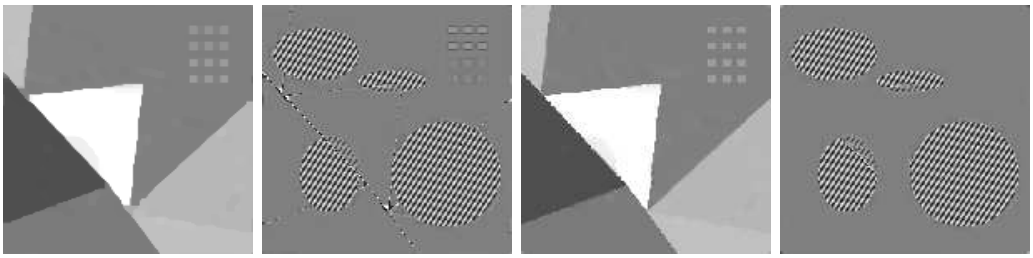

(d) Anisotropic TV + L2

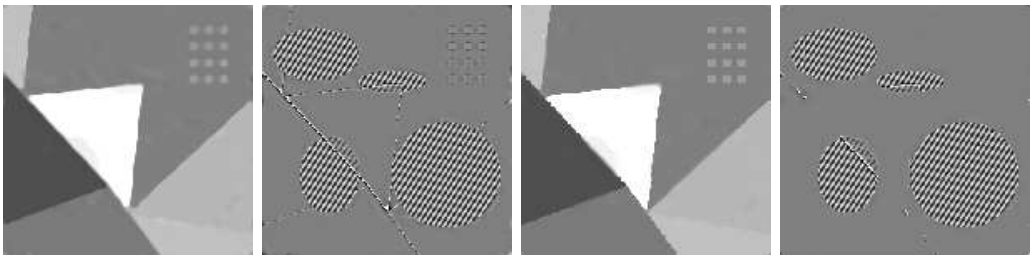

(e) Isotropic TV + L1

Figure 4.7: The first row corresponds to the BLMV filter. Two different σ values are used as it is noted. In the second, third, fourth row, the first and second columns correspond to the TV-Hilbert model and the third and fourth columns correspond to the proposed model. For a fair comparison, we use the same kernel K_σ and fix μ value.

Chapter 5

Conclusion and future works

In this dissertation, we proposed new variational models for image denoising and decomposition respectively. We now summarize the main results and introduce some remaining questions and future research directions.

In chapter 3, we studied appropriate regularizers based on TV and HOTV and proposed novel denoising model that uses a combination of a non-convex TV regularizer and a non-convex HOTV regularizer (non-convex hybrid TV model). Numerical experiments show that the non-convex hybrid TV model can restore a degraded image, preserve sharp edges, and facilitate smooth image intensity transitions without over-smoothing or over-sharpening. Although natural images consist of smooth regions, flat regions, jumps, and textures, the proposed non-convex hybrid TV model reconstructs these diverse characteristics of images effectively.

The proposed model can be extended for application to various image restoration problems, such as impulsive noise removal, image deblurring, image inpainting, and super-resolution. However, we did not address the convergence analysis of our iterative reweighted algorithm for solving $\min_u \|\nabla u\|_2^\alpha + \frac{\mu}{2}||u-f||^2$ and $\min_u \|\nabla^2 u\|_2^\alpha + \frac{\mu}{2}||u-f||^2$ with α <1, the characteristics of the solutions to the above problems, and the selection of the regularization parameter μ and norm $\|\cdot\|_2^\alpha$. These topics will be explored in future research.

In chapter 4, we focused on image decomposition. To preserve sharp edges on cartoon side in decomposing process, we modify the TV-Hilbert model, in

which we add the local gradient constraint. Based on the texture estimator, we construct the binary mask M. The local gradient constraint is incorporated into the model using this mask, which guides structural information such as edges to be preserved and oscillatory patterns to be smeared out in cartoon side.

To produce better decomposition results in current research, there remain several parameters which must be chosen properly for each image. How to reduce its parameters freedom for constructing a general decomposition model is a future research direction. Extending our decomposition model to design a texture-specific kernel will also be an interesting future work.

Blind deconvolution

Now, I would like to introduce more challenging topic in image restoration problem. We consider the problem of restoring a image blurred and contaminated by Gaussian noise.

Let Ω denote an open bounded set in R^2 on which the image intensity function $u : \Omega \to [0, 1]$ is defined. The standard linear degradation model is given by $f = k * u + n$, where f is the observed image, k is unknown shift-invariant blurring kernel, u is the original image we want to recover, n is the additive zero-mean Gaussian noise with standard deviation $\sigma \geq 0$, and $*$ stands for the convolution operator. In the case of color images, the image intensity is defined as $u : \Omega \to [0, 1]^3$. Here f^σ denotes the observed image at channel $\sigma \in \{r, g, b\}$ such that $f^\sigma = k * u^\sigma + n^\sigma$.

We approach the image restoration problem within the variational framework. We consider the following minimization problem in the unknown u and k,

$$\inf_{u,k}\{F(u, k) = \Phi(k * u - f) + \Psi_u(u) + \Psi_k(k)\},$$

where $\Phi(\cdot)$ is a functional representing the data-fidelity, and $\Psi_u(\cdot)$ and $\Psi_k(\cdot)$ are the regularization terms for alleviating the ill-posedness by enforcing the smoothness constraints on u and k respectively. Since we consider the Gaussian noise model, the L^2 -fidelity term led by the maximum likelihood estimation is used. For the impulsive noise, the L^1-fidelity term is useful. There exist many different types of regularization terms. I'm interested in

recovering u and k without any prior knowledge of the point spread function (PSF) and the image. This problem is called the blind deconvolution.

Since the number of unknowns exceeds the number of observed data, blind deconvolution using only a single image is an ill-posed problem. Many approaches have been devoted to handle technical issues arising from blind restoration such as general kernel, kernel refinement and large blur problem. Although we desire blind deconvolution model for a general kernel, blind deconvolution with a general kernel is ill-posed. Attempts to overcome this problematic issue can be classified into two categories. First way is to add relevant data. If multiple input images of the same scene can be available, the problem becomes more tractable. Second is to constrain the solution, in which the blurring kernel can be constrained to specific type or described as parametric functions.

To obtain sparse kernel and remove the noise, we can apply thresholding to the kernel estimation. But this operation ignores the inherent blur structure, possibly degrading the kernel quality. So, we need more efficient and high-quality kernel refinement.

The most algorithms work well for small blur but poorly work for large blur. To handle large blur, performing kernel estimation by varying image resolution in a coarse to fine manner is efficient. But theoretical analysis is not sufficient. Hence, based on existing researches, we need to exploit these technical issues and improve the quality of blind deconvolution.

Moreover, there remain material questions. Severe noise and saturation make the correct kernel estimation difficult. Even though we know a correct kernel, deconvolution of saturated image is still difficult. Most of existing blind deconvolution models assume the spatially invariant blur and are modeled by convolution operator. In real world cases, multiple relative motions caused by moving objects or depth difference from camera bring out the spatially variant blur. To deal with these limitations will be interesting future work.

Bibliography

[1] F. Andreu-Vaillo, V. Caselles, and J. M. Mazón, *Parabolic quasilinear equations minimizing linear growth functionals*, Cambridge, MA: Birkhauser (2004)

[2] G. Aubert and P. Kornprobst, *Mathematical problems in image processing : partial differential equations and the calculus of variations*, Springer: Applied Mathematical Sciences **147** (2006), 2nd ed.

[3] J.F. Aujol, G. Aubert, L. Blanc-Féraud and A. Chambolle, *Image decomposition into a bounded variation component and an oscillating component*, Journal of mathematical imaging and vision **22** (2005), no. 1, 71–88.

[4] J.F. Aujol and G. Gilboa, *Implementation and parameter selection for BV-Hilbert space regularization*, CAM Report 04-66, UCLA, Los Angeles, CA (2004).

[5] J. Aujol, G. Gilboa, T. Chan and S. Osher, *Structure-texture decomposition by a TV-Gabor model*, Lecture Notes in Computer Science **3752** (2005), 85–96.

[6] J.F. Aujol, G. Gilboa, T. Chan and S. Osher, *Structure-Texture image decompositon-modeling, algorithms, and parameter selection*, International journal of computer vision **67** (2006), no. 1, 111–136,

[7] L. Bar, A. Brook, N. Sochen and N. Kiryati, *Deblurring of color images corrupted by impulsive noise*, IEEE Trans. Image Process. **16** (2007), no.4.

[8] M. Benning, C. Brune, M. Burger and J. Muller, *Higher-order TV methods-Enhancement via Bregman iteration*, CAM Report 12-02, UCLA, Los Angeles, CA (2012).

[9] A. Blake and A. Zisserman, *Visual reconstruction*, Cambridge, MA:MIT Press (1987).

[10] P. Blomgren, T. Chan and P. Mulet, *Extensions to Total Variation denoising*, in Proceedings of SPIE, San Diego **3162** (1997), 367–375.

[11] E. Bollt, R. Chartrand, S. Esedoglu, P. Schultz and K. Vixie, *Graduated adaptive image denoising: local compromise between total variation and isotropic diffusion*, Advances in Computational Mathematics. **31** (2009), 61–85.

[12] K. Bredies, K. Kunisch and T. Pock, *Total generalized variation*, SIAM J. Imaging Sci. **3** (2010), no.3, 492–526.

[13] A. Buades, T. Le, J.M. Morel and L. Vese, *Fast cartoon + texture image filters*, IEEE Trans. Image Process. **19** (2010), no. 18, 1978–1986.

[14] M. Buckley, *Fast computation of a discretized thin-plate smoothing spline for image data*, Biometrika. **81** (1994), no. 2, 247–258.

[15] E. J. Candès, M. B. Wakin and S. P. Boyd, *Enhancing sparsity by reweighted L_1 minimization*, J. Fourier Analysis and Applications **14** (2008), no. 5, 877–905.

[16] A. Chambolle, *An algorithm for total variation minimization and applications*, Journal of Mathematical imaging and Vision **20** (2004), no.1-2, 89–97.

[17] A. Chambolle and P. Lions, *Image recovery via total variation minimization and related problems*, Numerische Mathematik **76** (1997), no.2, 167–188.

[18] A. Chambolle and T Pock, *A first-order primal-dual algorithm for convex problems with applications to imaging*, Journal of Mathematical Imaging and Vision **40** (2011), no. 1, 120–145.

[19] T. Chan and S. Esedoglu, *Aspects of total variation regularized L1 function approximation*, SIAM J. Appl. Math. **65** (2005), No. 5, 1817—1837.

[20] T. F. Chan, G. H. Golub and P. Mulet, *A nonlinear primal-dual method for total variation-based image restoration*, SIAM J. Sci. comput. **20** (1999), no.6, 1964–1977.

[21] T. Chan, A. Marquina and P. Mulet, *High-order total variation-based image restoration*, SIAM J. Sci. Comput. **22** (2000), no.2, 503–516.

[22] P. Charbonnier, L. B. Féraud, G. Aubert and M. Barlaud, *Deterministic edge-preserving regularization in computed imaging*, IEEE Trans.Image Process. **6** (1997), no. 2, 298—311.

[23] R. Chartrand, *Nonconvex regularization for shape preservation*, in Proceedings of IEEE International Conference on Image Processing (ICIP) **1** (2007), 293–296.

[24] R. Chartrand, *Exact reconstructions of sparse signals via nonconvex minimization*, IEEE Signal Process. Lett. **14** (2007), no. 10, 707–710.

[25] R. Chartrand and V. Staneva, *Restricted isometry properties and nonconvex compressive sensing*, Inverse Problems. **24** (2008), no. 3.

[26] R. Chartrand and W. Yin, *Iteratively reweighted algorithms for compressive sensing*, in Proceedings of the 33rd IEEE International Conference on Acoustics, Speech, and Signal Processing (ICASSP) (2008).

[27] X. Chen and W. Zhou, *Convergence of reweighted ℓ_1 minimization algorithms and unique solution of truncated ℓ_p minimization*, Technical Report, HK Polytech. Univ. (2010).

[28] M. Chipot, R. March, M. Rosati and G. V. Caffarelli, *Analysis of a nonconvex problem related to signal selective smoothing*, Math. Models Methods Appl. Sci. **7** (1997), no. 3, 313—328.

[29] P. Choudhury and J. Tumblin, *The trilateral filter for high contrast images and meshes*, In Proc. EGSR(Eurographics Symposium on Rendering) Eurographics (2003), 186–196.

[30] D. L. Donoho, *Compressed sensing*, IEEE Trans. Inform. Theory **52** (2006), no. 4, 1289–1306.

[31] K. Dabov, A. Foi, V. Katkovnik, K. Egiazarian, *Image denoising by sparse 3D transform-domain collaborative filtering*, IEEE Trans. Image Process. **16** (2007), no. 8, 2080–2095.

[32] Z. Farbman, R. Fattal, D. Lischinski and R. Szeliski, *Edge-preserving decompositions for multi-scale tone and detail manipulation*, ACM Transactions on Graphics **27** (2008), no. 3.

[33] R. Fergus, B. Singh, A. Hertzmann, S. T. Roweis and W. T. Freeman, *Removing camera shake from a single photograph*, ACM Trans. Graphics **25** (2006), no. 3, 787–794.

[34] T. Goldstein and S. Osher, *The split Bregman method for L1 regularized problems*, SIAM J. Imaging Sci. **2** (2009), no.2, 323–343.

[35] M. Hintermuller and T. Wu, *Nonconvex TV^q-models in image restoration: Analysis and a trust-region regularization based superlinearly convergent solver*, Institute of Mathematics and Scientific Computing, University of Graz. IFB-Report **52** (2011).

[36] P.W. Jones and T.M. Le, *Local scales and multiscale image decompositions*, Appl. comput. harmon. anal. **26** (2009), 371–394.

[37] S. Kim, S. Oh and M. Kang, *Mathematical image processing for automatic number plate recognition system*, J. KSIAM **14** (2010), no. 1, 57–66.

[38] F. Knoll, K. Bredies, T. Pock and R. Stollberger, *Second order total generalized variation (TGV) for MRI*, Magnetic Resonance in Medicine **65** (2011), 480-491

[39] D. Krishnan and R. Fergus, *Fast image deconvolution using hyper-Laplacian priors*, in Proceedings of the Advances in Neural Information Processing Systems (2009), 1–9.

[40] S. Lefkimmiatis, A. Bourquard and M. Unser, *Hessian-based norm regularization for image restoration with biomedical applications*, IEEE Trans. Image Process. **21** (2012), no. 3, 983–995.

[41] A. Levin, R. Fergus, F. Durand and W. T. Freeman, *Image and depth from a conventional camera with a coded aperture*, ACM Trans. Graphics. **26** (2007), no. 3, 70:1–70:9.

[42] A. Levin, Y. Weiss, F. Durand and W. T. Freeman, *Understanding and evaluating blind deconvolution algorithm*, in Proceedings of IEEE Conference on Computer Vision and Pattern Recognition. (2009), 1964–1971.

[43] F. Li, C. Shen, J.Fan and C. Shen, *Image restoration combining a total variational filter and a fourth-order filter*, Journal of Visual Communication and Image Representation. **18** (2007), no. 4, 322–330.

[44] M. Lysaker , A. Lundervold and X.-C. Tai, *Noise removal using fourth-order partial differential equation with applaication to medical magnetic resonance images in space and time*, IEEE Trans. Image Process. **12** (2003), no. 12, 1579–1590.

[45] M. Lysaker and X.-C. Tai, *Iterative image restoration combining total variation minimization and a second-order functional*, International Journal of Computer Vision **66** (2006), no. 1, 5–18.

[46] S.G. Mallat and Z. Zhang, *Matching pursuits with time-frequency dictionaries*, IEEE Trans. Signal Process. **41** (2003), no. 12, 3397–3415.

[47] A. Marquina and S. Osher, *Explicit algorithms for a new time dependent model based on level set motion for nonlinear deblurring and noise removal*, SIAM J. Sci. Comput. **22** (1999), 387–405.

[48] Y. Meyer, *Oscillating patterns in image processing and nonlinear evolution equations*, The Fifteenth Dean Jacqueline B. Lewis Memorial Lectures. Amer. Math. Soc., Boston, MA, USA. (2001).

[49] O. V. Michailovich, *An iterative shrinkage approach to total-variation image restoration*, IEEE Trans. Image Process. **20** (2011), no. 5, 1281–1299.

[50] M. K. Ng, R. H. Chan and W.-C. Tang, *A fast algorithm for deblurring models with Neumann boundary conditions*, SIAM J. Sci. Comput. **21** (1999), no. 3, 851–866.

[51] M. Nikolova, K. N. Michael, S. Q. Zhang and W. K. Ching, *Efficient reconstruction of piecewise constant images using nonsmooth nonconvex minimization*, SIAM J. Image Sci. **1** (2008), no. 1, 2–25.

[52] M. Nikolova, M. K. Ng and C.-P. Tam, *Fast nonconvex nonsmooth minimization methods for image restoration and reconstruction*, IEEE Trans. Image Process. **19** (2010), no. 12, 3073–3088.

[53] S. Oh, H. Woo, S. Yun and M. Kang, *Non-convex hybrid total variagion for image denoising*, Journal of Visual Communication and Image representation. (2013), 10.1016/j.jvcir.2013.01.010.

[54] S. Osher, A. Sole and L. Vese, *Image decomposition and restoration using total variation minimization and the $H^{-}1$ norm*, Multiscale Modeling and Simulation: A SIAM Inter-disciplinary Journal **1** (2003), no. 3, 349–370.

[55] Z.-F. Pang, L.-L. Wang and Y.-F. Yang, *The proximal point method for a hybrid model in image restoration*, arXiv:1110.1804v1 [cs.CV] (2011).

[56] K. Papafitsoros and C.-B. Schonlieb, *A combined first and second order variational approach for image reconstruction*, arXiv:1202.6341v1 [math.NA] (2012).

[57] P. Perona and J. Malik, *Scale-space and edge detection using anisotropic diffusion*, IEEE Trans. Pattern Anal. Mach. Intell. **12** (1990), no. 7, 629-–639.

[58] L. Qiegen, L. Jianhua and Z. Yuemin, *Adaptive image decomposition by improved bilateral filter*, International Journal of Computer Applications **23** (2011), no. 7, 16–22.

[59] L. Rudin, S. Osher and E. Fatemi, *Nonlinear total variation based noise removal algorithm*, Phys. D. **60** (1992), 259–268.

[60] Q. Shan, J. Jia and A. Agarwala, *High-quality motion deblurring from a single image*, ACM Trans. Graphics **27** (2008), no. 3, 73:1.–73:10.

[61] S. L. Su and F. Durand and M. Agrawala, *De-emphasis of distracting image regions using texture power maps*, Proceedings of the 4th ICCV Workshop on Texture Analysis and Synthesis (2005), 119–124.

[62] M. Tao and J. Yang, *Alternating direction algorithm for total variation deconvolution in image reconstruction*, Preprint (2009).

[63] M. W. Tao, M. K. Johnson and S. Paris, *Error-tolerant image compositing*, In European Conference on Computer Vision (ECCV) (2010).

[64] S. Teboul, L. Blanc-Féraud, G. Aubert and M Barlaud, *Variational approach for edge-preserving regularization using coupled PDE's*, IEEE Trans.Image Process. **7** (1998), no. 3, 387—397.

[65] R. Tibshirani, *Regression shrinkage and selection via the LASSO*, J. R. Statist. Soc. Ser. B. **58** (1996), no. 1, 267–288.

[66] A. Tikhonov and V. Arsenin, *Solutions of Ill-Posed Problems*, New York: Winston (1977).

[67] H. Tingbo, W. Sen and Q Hong, *Image deconvolution with multi-stage convex relaxation and its percenptual evalution*, IEEE Trans. Image Process. **20** (2011), no.12 , 3383–3392.

[68] C. Tomasi and R. Manduchi, *Bilateral filtering for gray and color images*, Proceedings of the IEEE International Conference on Computer Vision, Bombay, India. (1998).

[69] C. R. Vogel and M. E. Oman, *Iterative methods for total variation denoising*, SIAM J. Sci. Comput. **17** (1996), no. 1, 227–238.

[70] Z. Wang, A. C. Bovik, H. R. Sheikh and E. P. Simoncelli, *Image quality assessment: From error measurement to structural similarity*, IEEE Trans. Image Process. **13** (2004), no. 4, 600–612.

[71] Y. Wang, J. Yang, W. Yin and Y. Zhang, *A new alternating minimization algorithm for total variation image reconstruction*, SIAM J. Imaging Sci. **1** (2008), no. 3, 248–272.

[72] J. Weickert, *Anisotropic fiffusion in image Processing*, Teubner,Leipzig (1998).

[73] C. Wu and X.-C. Tai, *Augmented lagrangian method, dual methods and split bregman iteration for ROF, vectorial TV, and high order models*, SIAM J. Imaging Sci. **3** (2010), no. 3, 300–339.

[74] L. Xu , C. Lu , Y. Xu and J. Jia, *Image smoothing via L_0 gradient minimization*, ACM Trans. Graphics **30** (2011), no. 5, 174:1–174:12.

[75] Y. You and M. Kaveh, *Fourth order partial differential equations for noise removal*, IEEE Trans. Image Process.**9** (2000), no. 10, 1723-–1730

[76] J. Yuan, C. Schnörr and G. Steidl, *Total-Variation Based Piecewise Affine Regularization*, in Proceedings of the Second International Conference on Scale Space and Variational Methods in Computer Vision (2009), 552–564.

[77] T. Zhang, *Analysis of multi-stage convex relaxation for sparse regularization*, Journal of Machine Learning Research **11** (2010), 1081–1107.

[78] X. Zhang, M. Burger, X. Bresson and S. Osher, *Bregmanized nonlocal regularization for deconvolution and sparse reconstruction*, SIAM Journal on Imaging Sciences **3** (2010), no. 3, 253-276.

[79] W. Zhu and T. Chan, *Image denoising using mean curvature of image surface*, SIAM J. Imaging Sci. **5** (2012), no. 1, 1–32.

[80] S. Zhuo, D. Guo and T. Sim, *Robust Flash Deblurring*, IEEE Conference on Computer Vision and Pattern Recognition(CVPR) (2010)

[81] W. Zhu, X.-C. Tai and T. Chan, *Augmented Lagrangian method for a mean curvature based image denoising model*, CAM Report 12-02, UCLA, Los Angeles, CA (2012).

국문초록

영상복원은 과거 수십여년동안 영상 처리 분야와 컴퓨터 비전 분야에서 활발한 연구 분야이다. 우리는 영상 복원 문제의 변분법적 편미분방정식 모델을 다룬다. 우선 이 연구의 동기가 되는 고전적인 모델들을 탐구한다. 이 논문의 내용은 두 개의 주제로 나뉘어진다. 첫번째 주제는 영상잡음 제거이다. 비볼록 하이브리드 총변동 모델을 제시하고 반복 재가중치를 둔 알고리즘을 적용하여 제안한 모델의 해를 구한다. 두번째 주제는 영상 분할로서, 국소적 기울기 제한조건을 이용하여 영상을 구조성분과 진동성분으로 분해한다.

주요어휘: 영상 복원, 변분법, 오일러-라그랑즈 방정식, 잡음 제거, 영상 분할
학번: 2004-23262